"Assimilation of TOPEX/POSEIDON altimeter data into a global ocean circulation model: Are the results any good?"

by

Ichiro Fukumori

Ramanujam Raghunath

Lee-Lueng Fu

Yi Chao

Jet Propulsion Laboratory, California Institute of Technology, Pasadena CA 91109

July 2, 1998

Abstract

The feasibility of assimilating **satellite altimetry data** into a **global ocean general circulation model** is studied. Three years of **TOPEX/POSEIDON** data is analyzed using a global, three-dimensional, nonlinear primitive equation model. The assimilation's success is examined by analyzing its **consistency** and **reliability** measured by **formal error estimates** with respect to independent measurements. Improvements in model solution is demonstrated, in particular, properties not directly measured. Comparisons are performed with sea level measured by tide gauges, subsurface temperatures and currents from moorings, and bottom pressure measurements. Model representation errors dictate what can and cannot be resolved by assimilation and its identification is emphasized. *data assimilation*

1. Introduction

Data assimilation provides a means to estimate the state of the ocean from incomplete and sparse observations (Bennet, 1992; Wunsch, 1996), which characterize oceanographic measurements. The estimate is achieved by dynamically interpolating and extrapolating observations using theoretical relationships among properties embodied in models.

While data assimilation has become a mature tool for both research and application in meteorology, it is an emerging field in oceanography and much focus has hitherto been in theoretical investigations of methodology (see, for example, reviews by Ghil and Malanotte-Rizzoli [1991] and Anderson et al. [1996]). Methods based on statistical correlation (e.g., Ezer and Mellor, 1994) and quasi-geostrophic dynamics (e.g., Haines, 1991) have been explored to map observations onto model fields. Approximations in estimation theory have been advanced to overcome computational requirements of Kalman filtering (e.g., Fukumori et al., 1993, 1995; Cane et al., 1996; Evensen, 1994). Significant progress has been made in automatic adjoint code generation (Giering and Kaminski, 1998) which together with advances in computational power have enabled adjoint methods to be applied to large-scale problems (e.g., Stammer et al., 1997).

It is often taken for granted that assimilated estimates are more accurate than non-assimilated model results. However, the accuracy of the estimation critically depends on the reliability of the underlying assumptions, implicit and/or explicit. In principle, if the assumptions are correct and the problem is solved consistently with

such assumptions, an assimilated estimate should be more accurate than one without assimilation in every aspect of the solution, or at least no worse than such, including properties not directly measured by the data. For instance, a solution based on assimilation of altimeter data should produce better (at least not worse) temperature and velocity fields throughout the water column.

The purpose of this study is to test this assertion by assimilating the TOPEX/ POSEIDON altimeter data into a global, three-dimensional, nonlinear primitive equation model. Although global in coverage, satellites only measure properties of the sea surface, whereas ocean circulation is inherently three-dimensional. In addition, the nature of ocean circulation associated with large-scale sea level changes is spatially and temporally inhomogeneous (e.g., Fukumori et al., 1998) making ocean estimation from altimetry nontrivial. Various measures are explored to assess the goodness and success of the assimilation. The results are compared to observations, both the ones that have been assimilated and those not included in the assimilation, for testing the degree of improvement made by the assimilation over pure simulation without assimilating any data. The assimilation's consistency and accuracy are examined with respect to formal uncertainty estimates. In particular, assumptions are clarified to explicitly identify the nature of the estimate, in terms of what is and is not resolved by the calculation. The problem, as it will be shown, in essence concerns identification and specification of uncertainties in both model and data, which are often assumed to be given in theoretical studies of assimilation methods.

The manuscript is organized as follows. The model and data are briefly described in sections 2 and 3, respectively. The assimilation scheme together with its assumptions are discussed in section 4, and the results' consistency is analyzed by various measures in section 5. A summary and discussion is presented in section 6. The paper ends with concluding remarks in section 7.

2. Model

The model used in this study is the same as that used by Fukumori et al. (1998) and is based on the Modular Ocean Model version 1.0 developed by the Geophysical Fluid Dynamics Laboratory of the National Oceanic and Atmospheric Administration (Pacanowski et al., 1991). The model is a nonlinear primitive equation model using the Boussinesq and rigid lid approximations. The model domain extends over the world

ocean from 80°S to 80°N with a uniform spatial resolution of 2° longitude and 1° latitude. There are 12 vertical levels (Table 1), which are chosen to coincide with the inflection points of the eleventh baroclinic mode of horizontal velocity corresponding to the mean temperature-salinity profile of the global ocean (Levitus, 1982). This choice is an attempt to make the vertical grids resolve vertical scales uniformly with respect to the mean stratification for a given number of vertical levels. The model has realistic topography and coast lines as shown in Figure 1. All horizontal boundaries are treated as impermeable with no-slip boundary conditions. Conventional Laplacian operators are used for horizontal and vertical mixing. Horizontal viscosity and diffusivity are set constant with values of 2×10^8 and 2×10^7 cm^2/s, respectively. Vertical mixing coefficients are based on the Richardson number formulation of Pacanowski and Philander (1981), with an additional local vertical mixing performed to remove any statically unstable profiles.

The model is first spun up for 8 years forced by climatological monthly winds (Hellerman and Rosenstein, 1983) and by relaxation (30-day time-scale) of its surface temperatures and salinities to monthly Levitus' (1982) values. The initial condition is at rest with a temperature and salinity distribution of Levitus (1982). Following the 8-year spinup, the model is forced by daily surface winds and climatological monthly heat flux from January 1992 to December 1995. The winds and heat flux are based, respectively, on the National Center for Environmental Prediction's (NCEP) 1000 mbar analysis using the formula of Wu (1982) and on the Comprehensive Ocean-Atmosphere Data Set (COADS) (Slutz et al., 1985; Woodruff et al., 1987) compiled by da Silva et al. (1994).

A linear trend is computed and removed from all results of the model calculation (Fukumori et al., 1998). Such trend arises primarily because the model's thermal forcing during the real-time run (as opposed to spin-up) has no relaxation terms; Incompatibilities between oceanic heat flux and the prescribed surface flux during the relatively short simulation lead to secular changes in ocean circulation. However, their effects are local for short periods of time as conducted in this study, and therefore subsequent analyses will focus on the variabilities with respect to this trend.

3. TOPEX/POSEIDON Data

Global sea level anomalies measured by TOPEX/POSEIDON (T/P) from January 1, 1993 to December 31, 1995 are analyzed. Data are based on the merged T/P Geophysical Data Record (GDR) with all standard environmental corrections applied including solid earth and ocean tides, water vapor, dry tropospheric and ionospheric delays, and an inverse barometer correction for atmospheric pressure loading of the sea surface. Oceanic tidal correction is based on the University of Texas model (Eanes and Bettadpur, 1996), and the inverse barometer correction takes into account the temporal changes in global mean atmospheric pressure (Ponte, 1993). Temporal variabilities (sea level anomalies) are computed relative to the 3-year mean sea level to avoid uncertainties associated with the marine geoid. Time-continuous, along-track measurements will be used directly in the analysis as opposed to space-time maps of the data, to avoid possible aliasing of high frequency barotropic signals at high latitudes (Fukumori et al., 1998). However, in light of the coarse resolution of both model (Section 2) and assimilation scheme (Section 4), and to limit the volume of the raw data set, the T/P measurements were averaged along-track into 2.5° latitudinal bins. Finally, linear trends in measured sea level were computed and removed from the binned T/P data, because trends which are not resolved by the present model (Section 2) would require modifications to the assimilation scheme otherwise (Gelb, 1974).

4. Approximate Kalman Filter and Smoother

The assimilation in this study employs an approximate Kalman filter and smoother based on a time-asymptotic and a reduced-state approximation (Fukumori et al. [1991], Fukumori and Malanotte-Rizzoli [1995]). In short, the two approximations simplify the evaluation of the estimation's error covariance matrix so as to minimize the computational requirements of Kalman filtering. The asymptotic approximation employs the time asymptotic limit of the Riccati equation rather than evaluating a time-evolving error estimate. The reduced-state approximation seeks to represent the error covariance with fewer degrees of freedom than those of the model's prognostic variables. The representation is carefully chosen to resolve the dominant structures of the error.

The two approximations would formally lead to suboptimal estimates; However, given the uncertainties in our knowledge about the exact nature of the data error and process noise (e.g., their structural and temporal dependence), the results may be

4

statistically indistinguishable from truly optimal estimates (Cane et al., 1996). The virtue of the approximations lies in rendering the quantitative framework of Kalman filtering feasible, allowing objective evaluation of the estimation error covariances. For instance, estimation errors are typically anisotropic and inhomogeneous with nontrivial covariances among different properties that are otherwise difficult to specify. As shown below and in the next section, the error covariances define the assimilation problem itself and dictates the goodness of the assimilated solution. The objective formulation of the Kalman filter assures the accuracy and consistency of the resulting assimilation.

4.1 State Reduction

A natural basis set for approximating the filter is identified by examining properties of sea level. Using the same model as in the present study, Fukumori et al. [1998] recently investigated the nature of large-scale sea level variability. Despite the enormous degrees of freedom present in such general circulation models, only a handful of processes are found to dominate sea level variability. In the tropics (latitude $\phi <$ 20°), low-frequency (> 100 days) wind-driven baroclinic changes are dominant with the first baroclinic mode contributing most of the variance. Variability associated with high-frequency wind-driven barotropic motion are the largest sea level signal at high latitudes ($\phi >$40°), accounting for as much as half the variance in periods shorter than 20-days. In mid-latitudes (20°$< \phi <$40°), near-surface steric effects due to seasonal heating and cooling are found to dominate sea level variance. However, to first approximation, large-scale seasonal heating and cooling affect local heat storage but have relatively small dynamic effects (Gill and Niiler [1973]). Therefore, a leading approximation for the dynamics of global large-scale sea level change is attained in terms of the barotropic and first baroclinic modes alone.

The approximate filter is computed relative to the time-mean state of the model simulation. Although variable topography and nonlinearities render the equations of motion nonseparable into independent vertical modes, and thus each mode is dependent on another, dynamic normal modes locally form a complete set of orthogonal vertical basis functions with which variables can be expanded. The model's transport stream function (ψ) conveniently defines the barotropic mode. The baroclinic component is defined by amplitudes of the model state anomalies projected onto the first baroclinic mode. Vertical displacement is used as one of the baroclinic variables instead of temperature and salinity, because of the adiabatic nature of wind-driven sea level change.

In summary, the model's prognostic variables, zonal (u) and meridional velocity (v), temperature (T), and salinity (S), are approximated by

$$(u, v, T, S) \approx (\overline{u}, \overline{v}, \overline{T}, \overline{S}) + (-\frac{1}{H}\frac{\partial \psi}{\partial y} + a_u \hat{p}, \; \frac{1}{H}\frac{\partial \psi}{\partial x} + a_v \hat{p}, \; a_d \hat{h}\frac{\partial \overline{T}}{\partial z}, \; a_d \hat{h}\frac{\partial \overline{S}}{\partial z}) \quad (1)$$

where overbar denotes the reference state, and $\hat{p}$ and $\hat{h}$ are structures of first baroclinic modes of velocity and displacement defined locally, respectively (e.g., Gill, 1982). Coefficients a_u, a_v, a_d denote first baroclinic mode amplitudes of zonal and meridional velocity, and vertical displacement, respectively, and are functions of horizontal location.

Prospects of reducing the horizontal degrees of freedom are assessed by examining scales of variability. Empirical orthogonal functions (EOFs) were computed based on correlation of model sea level over the entire domain. The correlation matrix instead of the covariance matrix is used to derive EOFs, so as to identify the dominant scales of correlation rather than structures of dominant variance. The first two modes describe the annual period and dominate the overall variability (38% of the total), while the next 297 EOFs are found necessary to explain 99% of the remaining correlation.

Figure 2 shows typical examples of the structure of the resolution matrix (see, for example, Fukumori and Malanotte-Rizzoli [1995]) that in effect describes the scales of variability. Based on such structures, a coarse grid was defined with a uniform 10° by 5° zonal and meridional grid spacing, respectively, so as to resolve the dominant scales. Objective mapping (Bretherton et al., 1976) is used to map values on this coarse grid onto the finer model grid, thus defining the coarse-to-fine grid transformation for the reduced-state filter. A Gaussian correlation function is used with correlation distance of 7.5° zonally and 3.75° meridionally (75% of the coarse grid spacing). Distances between any two points are computed along great circles unless a land mass is present in between, in which case it was computed around the land perimeter. Therefore, for example, correlation across the Isthmus of Panama is nil, even though the direct distance is small.

An inverse transform that maps variables on the model's horizontal grid onto the coarse grid was computed as the pseudo inverse of this objective mapping operator. Figure 3 compares sea level anomaly at a particular instant with its coarse approximation; The similarities between the fine and coarse representation demonstrates the fidelity of the transformation as well as the large-scale nature of model sea level.

The same mapping operator is used for all coarse grid state elements, except for differences due to relative grid location (B-grid) and for stream function. For the latter, mapping is performed so as to satisfy the horizontal boundary condition of no normal flow into boundaries. This is achieved by solving the corresponding vorticity equation following the above objective mapping operation.

4.2 Model Representation Error

The Kalman filter in essence is an inversion of model equations based on relative accuracies of model and data (e.g., Gelb, 1974). One of the primary virtues of Kalman filtering is in its objective framework of evaluating errors as part of the estimate. However the so-called Riccati equation that describes the evolution of such errors involves data error and model process noise, of which both must be specified a priori. It is instructive to identify the exact nature of these errors for any assimilation problem, whether solved by the Kalman filter or otherwise, because such error specification defines the inverse problem itself. The nature of model and data errors are identified below first for the full estimation problem, and then followed by the equivalent under the reduced-state approximation.

Data assimilation is typically set up in terms of a least-squares estimate ($\mathbf{x}$) that minimizes the following cost function J;

$$J = \Sigma_t(\mathbf{y} - \mathbf{H(x)})^T \mathbf{R}^{-1}(\mathbf{y} - \mathbf{H(x)}) + \Sigma_t(\mathbf{x} - \hat{\mathbf{x}})^T \mathbf{P}^{-1}(\mathbf{x} - \hat{\mathbf{x}}) \qquad (2)$$

Here, $\hat{\mathbf{x}}$ is the model's true state to be defined presently, $\mathbf{y}$ is the data, $\mathbf{H(x)}$ is the model equivalent of the data, and the weights $\mathbf{R}$ and $\mathbf{P}$ are the error covariance matrices of data and model, respectively (e.g., Wunsch, 1996). Proper specification of these weights is essential to the optimality of the solution because a mis-specification by definition amounts to solving a different problem. Cohn (1997) describes the exact nature of these error covariances and is summarized below.

First, it is essential to recognize the fundamental difference between the ocean and the model. Models have finite dimensions whereas the real ocean has infinite degrees of freedom. The relation between the real ocean ($\mathbf{w}$) and the model's true state ($\hat{\mathbf{x}}$) could be expressed functionally as;

$$\hat{\mathbf{x}} = \Pi\mathbf{w} \qquad (3)$$

The operator Π relates the complete and exact state of the ocean to its representation in the finite and approximate space of the model. Such operator includes both spatial averaging as well as truncation and/or approximation of the physics. For instance, finite dimensional models lack scales smaller than its grid resolution. Quasi-geostrophic models resolve neither inertial waves nor tides. Then, 'model error' is the difference between a given model state and the true state defined by (3),

$$\mathbf{x} - \hat{\mathbf{x}} = \mathbf{x} - \Pi\mathbf{w} \tag{4}$$

the expected covariance of which is $\mathbf{P}$ (Eq 2).

'Data error' also requires some consideration. Observations $\mathbf{y}$ measure properties of the real ocean and can be described symbolically as;

$$\mathbf{y} = \mathbf{E}(\mathbf{w}) + \epsilon \tag{5}$$

where $\mathbf{E}$ represents the measurements' sampling operation and ϵ denotes measurement errors. Function $\mathbf{E}$ is generally different from the model equivalent, $\mathbf{H}$, owing to the differences between $\mathbf{x}$ and $\mathbf{w}$ (Eq 3). Measurement errors are strictly instrumental errors of the observation, and represent quantities unrelated to either the model or the ocean. For satellite altimetry, ϵ includes, for example, errors in the satellite's orbit and ionospheric corrections.

In terms of quantities in model space, equation (5) can be rewritten as;

$$\mathbf{y} = \mathbf{H}(\hat{\mathbf{x}}) + \{\mathbf{E}(\mathbf{w}) - \mathbf{H}(\Pi\mathbf{w})\} + \epsilon \tag{6}$$

Assimilation is the inversion of (6) that relates model state to observations rather than a solution of (5). The second term on the right-hand-side of (6) describes differences between the ocean and the finite dimension of the model, and is termed model representation error. Representation errors correspond to processes affecting observations but missing from the model, and, as far as the model inversion is concerned, is indistinguishable from instrument error. Representation errors are inconsistent with model physics and are typically, but not necessarily, quantities whose scales are smaller than model grid spacing. Being inconsistent with the model, representation errors are not correctable by assimilation.

Representation error and instrument noise together constitute uncertainties relating observations and model state, and for a lack of a better word, are collectively

called 'data error' with its expected covariance being $\mathbf{R}$ in Eq (2). In effect, representation errors downweight the data constraint (Eq 2) and prevent a model from being forced too close to observations that it cannot represent, thus guarding against model 'indigestion'.

Under the reduced state approximation, the model state and its errors are divided into contributions from the range and null space of the state reduction transformation; e.g.,

$$\mathbf{x} = \mathbf{x}_r + \mathbf{x}_n \tag{7}$$

(Subscripts r and n denote the range and null space of the state reduction operator, respectively.) The reduced-state filter solves the optimization problem (2) in terms of the reduction's range space, by approximating the model error (4) with its range subspace;

$$\mathbf{x}_r - \hat{\mathbf{x}}_r \approx \mathbf{x} - \Pi\mathbf{w} \tag{8}$$

The model state's null space part of the state reduction, $\mathbf{x}_n$, is unconstrained by the approximate filter and its errors contribute to 'data error'. Namely, under the reduced-state filter, model data differences are computed in the total model space (Fukumori and Malanotte-Rizzoli, 1995) and Eq (6) is solved as,

$$\mathbf{y} = \mathbf{H}(\hat{\mathbf{x}}_r) + \mathbf{H}(\mathbf{x}_n) + \{\mathbf{E}(\mathbf{w}) - \mathbf{H}(\Pi\mathbf{w})\} + \epsilon \tag{9}$$

The first term in (6) is rewritten in terms of the unknown range part of the true model state $(\hat{\mathbf{x}}_r)$ plus the unconstrained null space part $(\mathbf{x}_n)$. The approximate filter in effect inverts the first term of (9). Uncertainties of the second term, viz., errors in the state transformation's null space, therefore constitute part of the uncertainties of Eq (9) in addition to the model's 'data error'.

4.3 Error Specification

Equations (4) and (6) identify errors for the assimilation problem, but do not by themselves describe the errors' magnitude or structures. Fu et al. (1993) introduced an objective approach in assigning actual values for such errors. Here, we shall write down the equivalent equations for the reduced state filter. The observation, $\mathbf{y}$, and its

simulation (model equivalent), $\mathbf{m}$, can be written in terms of the true signal plus their respective errors;

$$\mathbf{y} = \mathbf{s}_r + \mathbf{s}_n + \mathbf{r} \tag{10}$$

$$\mathbf{m} = (\mathbf{s}_r + \mathbf{p}_r) + (\mathbf{s}_n + \mathbf{p}_n) \tag{11}$$

$$\mathbf{m}_r = \mathbf{s}_r + \mathbf{p}_r \tag{12}$$

where $\mathbf{s}$ and $\mathbf{p}$ are signal and simulation errors, respectively. $\mathbf{r}$ is data error and is the sum of instrument error plus model representation error (Eq 6). Subscripts r and n denote the range and null space of the state reduction operator, respectively. Assuming the signals and the two errors, and the range and null space of the state reduction are mutually independent, the covariance among the data and simulation are;

$$< \mathbf{y}\mathbf{y}^T > \; = \; < \mathbf{s}_r \mathbf{s}_r^T > + < \mathbf{s}_n \mathbf{s}_n^T > + < \mathbf{r}\mathbf{r}^T > \tag{13}$$

$$< \mathbf{m}\mathbf{m}^T > \; = \; < \mathbf{s}_r \mathbf{s}_r^T > + < \mathbf{p}_r \mathbf{p}_r^T > + < \mathbf{s}_n \mathbf{s}_n^T > + < \mathbf{p}_n \mathbf{p}_n^T > \tag{14}$$

$$< \mathbf{m}_r \mathbf{m}_r^T > \; = \; < \mathbf{s}_r \mathbf{s}_r^T > + < \mathbf{p}_r \mathbf{p}_r^T > \tag{15}$$

The covariance of the residuals (model data difference) are,

$$< (\mathbf{y} - \mathbf{m})(\mathbf{y} - \mathbf{m})^T > \; = \; < \mathbf{r}\mathbf{r}^T > + < \mathbf{p}_r \mathbf{p}_r^T > + < \mathbf{p}_n \mathbf{p}_n^T > \tag{16}$$

$$< (\mathbf{y} - \mathbf{m}_r)(\mathbf{y} - \mathbf{m}_r)^T > \; = \; < \mathbf{r}\mathbf{r}^T > + < \mathbf{p}_r \mathbf{p}_r^T > + < \mathbf{s}_n \mathbf{s}_n^T > \tag{17}$$

From these equations, the reduced state's simulation error and the effective data error (Eq 9) can be estimated by,

$$< \mathbf{p}_r \mathbf{p}_r^T > = \{ < (\mathbf{y} - \mathbf{m}_r)(\mathbf{y} - \mathbf{m}_r)^T > + < \mathbf{m}_r \mathbf{m}_r^T > - < \mathbf{y}\mathbf{y}^T > \}/2 \tag{18}$$

$$\begin{aligned} < \mathbf{r}\mathbf{r}^T > + < \mathbf{p}_n \mathbf{p}_n^T > = \; & < (\mathbf{y} - \mathbf{m})(\mathbf{y} - \mathbf{m})^T > \\ & - \{ < (\mathbf{y} - \mathbf{m}_r)(\mathbf{y} - \mathbf{m}_r)^T > + < \mathbf{m}_r \mathbf{m}_r^T > - < \mathbf{y}\mathbf{y}^T > \}/2 \end{aligned} \tag{19}$$

respectively. The right hand side of (18) and (19) can be estimated by comparing T/P observations with results of the simulation, substituting temporal averages for statistical ensemble means. Plates 1a and 1b, show results of such computation. Data error is the dominant component ($\mathbf{r}$), and is in fact much larger than the measurement accuracy of T/P, which is about 2 to 3 cm rms. Such excess data error is due to the coarse nature of the model (and to a lesser extent that of the filter), which limits the

model's ability in simulating mesoscale eddies. Sea level variance due to mesoscale eddies are part of the model's representation error and should therefore be included in data error (Eq 6). In fact much of the data error estimate's structure (Plate 1a) reflects the spatial distribution of mesoscale variability.

The model's incremental error, i.e., process noise, was modeled in the form of wind error with covariance proportional to the sample covariance of NCEP winds used in forcing the model. This assumption, however, should not be literally interpreted as model errors being dominated by wind errors. Rather it is merely an assumption of a particular form of model process noise (e.g., Miller and Cane, 1989). The magnitude of process noise is calibrated such that the corresponding error estimate of the simulated state (solution of the Lyapunov Equation [e.g., Stengel, 1986]) would be comparable with those based on Eq (18) (Plate 1b) (Fu et al., 1993; Menemenlis and Chechelnitsky, 1998). Plates 1c and 1d show such calibrated process noise and corresponding simulation error estimates, respectively.

4.4 Structures of the Kalman Gain

The approximate Kalman filter is defined by a time-asymptotic error covariance matrix of the assimilated state. Such limit is computed assuming a stationary observing system in addition to the calibrated data error and process noise estimated above. Data distribution during one three-day period was used as a representative set of regular observations as in Fukumori (1995), taking advantage of the three-day subcycle of T/P. Namely, the approximate estimation error covariance matrix is computed assuming data at locations during one particular subcycle of T/P being instantaneously assimilated every three-days. Note however, that actual assimilation, while employing the resulting time-invariant state error covariance matrix, correctly accounts for the time-varying data distribution; i.e., both $\mathbf{H}$ and $\mathbf{R}$ are time-varying in the Kalman filter (Fukumori, 1995).

To gain some insight into the nature of the Kalman filter's inversion, Plate 2 examines how the filter distributes model changes vertically in terms of their contribution to sea level. Namely, the figure shows model sea level anomalies at each grid point corresponding to the filter's changes in first baroclinic and barotropic circulation under a 1 cm instantaneous model-data difference at that location.

Plate 2 shows the filter interpreting model sea level errors as errors primarily in baroclinic circulation in the tropics and barotropic circulation away from the equator,

11

consistent with the general nature of sea level variability (Fukumori et al., 1998) and the assumed form of model process noise (i.e., wind). The sea level changes themselves are much smaller than the assumed model-data difference of 1 cm; This is due to uncertainties of the data on one hand (Plate 1a) and the accuracy of the model achieved by accumulating information from past observations on the other.

The horizontal structure of the Kalman gain (Figure 4) is mostly local, in a sense that the influence of a single data point is geographically confined resulting in a typical "bull's eye" structure for model correction. However, the influence radius is often anisotropic and inhomogeneous due to differences in local dynamics. For instance, the Antarctic Circumpolar Current (ACC) and the presence of the mid-ocean ridge elongates stream function changes in the Southern Ocean in the east-west direction (Figure 4a). Baroclinic changes at the same location, although small in terms of its contribution to sea level, also have significant side-lobes along the path of the ACC (Figure 4c). Changes in stream function are typically associated with dipolar structures near continents due to boundary conditions, but also exhibit similar structures near the Equator (Figure 4b) because of the Equator acting as a boundary due to change in sign of the Coriolis parameter. The sign of the stream function changes are also different at the assumed data points across the Equator (Figures 4a and 4b) due to the sign of the Coriolis parameter. Significant side-lobes also occur in baroclinic changes along the Equator reflecting Equatorial wave dynamics. Changes along the Equator (Figure 4d) are similar to the effects of local wind-forcing, which forces a Kelvin wave with temperature and zonal velocity anomalies centered on the equator, and an associated Rossby wave of opposite phase to the west of the Kelvin wave with off-equatorial maxima.

5. Validation

Data assimilation, particularly under the so-called weak constraint (Sasaki, 1970), is a rank deficient inverse problem. There exist an infinite number of solutions that could reduce the model–data difference to an arbitrary magnitude, and therefore the accuracy of the result must be carefully assessed. Such assessment can be achieved by examining self-consistencies of the assimilated estimate and by comparing results with independent observations. All estimates discussed below are smoothed estimates (e.g., Fukumori, 1995) unless otherwise noted.

5.1 Self Consistency

We examine the solution's consistency with respect to the statistical assumptions underlying the assimilation by comparing residuals of the inversion to corresponding error estimates. Because model residuals are dominated by data error (section 4.3), the skill is best compared among different model estimates; simulation (subscript sim), forecast (argument $-$), and filtered analysis. The forecast is the estimate immediately prior to the recursive assimilation of the observations. Based on the following relation (e.g., Gelb, 1974);

$$< (\mathbf{y} - \mathbf{Hx}_{sim})(\mathbf{y} - \mathbf{Hx}_{sim})^T > = \mathbf{R} + \mathbf{HP}_{sim}\mathbf{H}^T \tag{20}$$

$$< (\mathbf{y} - \mathbf{Hx}(-))(\mathbf{y} - \mathbf{Hx}(-))^T > = \mathbf{R} + \mathbf{HP}(-)\mathbf{H}^T \tag{21}$$

$$< (\mathbf{y} - \mathbf{Hx})(\mathbf{y} - \mathbf{Hx})^T > = \mathbf{R} - \mathbf{HPH}^T \tag{22}$$

the skills of the dynamic forecast ($\mathbf{x}(-)$) relative to simulation ($\mathbf{x}_{sim}$), and those of the filtered estimate ($\mathbf{x}$) relative to the forecast ($\mathbf{x}(-)$) are,

$$< (\mathbf{y} - \mathbf{Hx}_{sim})(\mathbf{y} - \mathbf{Hx}_{sim})^T > - < (\mathbf{y} - \mathbf{Hx}(-))(\mathbf{y} - \mathbf{Hx}(-))^T > =$$
$$\mathbf{HP}_{sim}\mathbf{H}^T - \mathbf{HP}(-)\mathbf{H}^T \tag{23}$$

and

$$< (\mathbf{y} - \mathbf{Hx}(-))(\mathbf{y} - \mathbf{Hx}(-))^T > - < (\mathbf{y} - \mathbf{Hx})(\mathbf{y} - \mathbf{Hx})^T > = \mathbf{HP}(-)\mathbf{H}^T + \mathbf{HPH}^T \tag{24}$$

respectively. The former measures the ability of the model in retaining and propagating data information consistently in time whereas the latter quantifies the measurements' effect in correcting the model at the instant of each measurement.

Plate 3 compares estimates of the left- and right-hand sides of Equations 23 and 24 by substituting temporal averages in place of statistical expectations. The agreement is remarkably good for both estimates in terms of overall magnitude and spatial structure. The filtering process has improved the model globally, and particularly in the Equatorial Indian Ocean ($\sim 15°$S), the tropical Pacific, the western tropical Atlantic, and the Bellingshausen Abyssal Plain.

The skill of the forecast $\mathbf{x}(-)$ (Eq 23) compares the assimilated estimate with data not yet used and therefore provides one test of the assimilation against independent

observations. In particular, the fact that the forecast skill is better than that of the simulation almost everywhere (Plate 3a) further demonstrates the assimilated estimate's reliability. Regions where the forecast skill is worse than that of simulation are few and patchy with many coinciding with regions associated with large meso-scale variability, such as the Agulhas Current and the Kuroshio Extension. Inaccuracies of assumptions, such as missing physics being white in both space and time, likely outweigh the large-scale signal extracted by the assimilation in such regions.

5.2 Tide Gauge Records

The model sea level estimates were compared with WOCE fast delivery tide gauge data, made available from the University of Hawaii Sea Level Center (Figure 5). Comparisons are restricted to stations where distances to the closest model grid point are less than 300 km. Stations were also limited to those having daily sea level data available for at least 550 days over the 3-year modeling period. Among 90 such available gauges, 65 (shown as empty circles in Figure 5a) have smaller sea level differences with the T/P assimilated estimates than with model simulation without data assimilation, demonstrating improvements made by the assimilation.

On the other hand, tide gauges that have larger model–data differences after T/P assimilation (solid circles) indicate places where the estimation is inaccurate, either due to errors in the estimation process or unaccounted physics dominating tide gauge records. Mitchum (1994) performed a comprehensive comparison between tide gauge measurements and T/P data. In particular stations at Socorro (18°N, 111°W) and Fort Point (37°N, 122°W) did not compare well with nearby altimetric measurements. Indeed sea level at these stations are hardly improved by the altimetric assimilation, suggesting that these stations do not represent sea level in the open ocean well.

Mitchum (1994) found that the differences in the exact location of some of the tide gauge stations and T/P ground points were important in reconciling the two measurements because of the presence of large amplitude short-scale planetary waves. These stations include Noumea (22°S, 166°E) and French Frigate Shoals (24°N, 166°W). Because the approximate filter and smoother are designed only to resolve large-scale variability, the present T/P assimilation is not able to improve estimates at stations dominated by short-scale physics, as found at these stations.

Comparisons of the assimilated results with in situ measurements depend on how representative the latter is of the larger scale circulation. Based on T/P data sampled at 25 km along-track resolution, Mitchum (1994) generally found good agreement between tide-gauges and T/P data, except for the stations described above. He also demonstrated that the agreement with coastal tide gauge measurements is generally less than with island stations. In fact most of the stations with larger model–data differences resulting from assimilation are found along continental margins which are actually outside the model domain due to the model's coarse resolution.

To examine the large-scale representativeness of sea level measured by individual tide gauge stations, the latter data were compared with the gridded T/P observations used in the assimilation (Figure 5b). Again, comparisons were restricted between stations and altimeter data within 300 km of each other. This comparison differs from Mitchum's (1994) in that comparisons are made with average T/P data within a 300 km radius of the tide gauges (in addition to the 2.5° latitudinal averaging described in section 3) rather than the closest altimeter ground point at the same latitude, and inverse barometer corrections are applied for both altimetry and tide gauge data.

Many gauges with insignificant correlation with T/P observations (solid dots in Figure 5b) coincide with those that show lack of improvement by the T/P assimilation (Figure 5a), suggesting that short-scale processes near these stations dominate tide gauge records that are not adequately resolved by the assimilation. In particular, large deficiencies of the model along the northwestern coast of North America are noted, where the California Current system is known to have large variations over relatively small scales.

5.3 Current Meter Data

Table 2 summarizes a comparison between model estimates and near surface current meter data from the Tropical Atmosphere Ocean (TAO) array located along the Equator in the Pacific Ocean. As measured by correlation and residual variance, the zonal velocity of the model simulation is generally in better agreement with in situ measurements than the meridional component is. Likewise, the assimilation shows more improvement in zonal than meridional velocity at these locations. For instance, at 140°W 45m-depth (Plate 4a) the simulation resolves the dominant low frequency variation with time-scales of several hundred days, but significantly differs from the observations

15

from day 1000 to 1100. The altimetric assimilation corrects this major error as well as reduces discrepancies during other periods.

On the other hand, the assimilation results in degradation of the zonal velocity estimates with respect to in situ measurements near the surface at 110°W and towards the bottom of the current meter array at 165°W. A closer examination shows that these degradations appear to be due to processes that are local and unresolved by the model, i.e., representation error. For instance, zonal velocity changes at 45m 110°W (Plate 4b) are dominated by a low-frequency event from day 800 to 1300, which is qualitatively lacking from the model. Such anomalies are also absent from measurements at either 120m 110°W (Plate 4c) or 45m 140°W (Plate 4a).

The meridional component shows little improvement by the assimilation, in particular at 140°W where the model simulation itself demonstrates little skill. Plate 4d compares meridional velocity among the estimates at 140°W 25m-depth. As is typical for in situ measurements, meridional velocity at the Equator is dominated by oscillations with amplitudes as large as 50 cm/s and time-scale on the order of 20-days (Halpern et al., 1988). Although the model exhibits similar oscillations, they are incoherent with in situ measurements and their amplitudes are much smaller, which again indicates a non-random error consistent with missing model physics rather than model state error.

5.4 Subsurface Temperature

TAO's temperature measurements offer additional means of model validation. Plate 5 shows examples of comparing TAO temperature anomalies with model estimates. At 8°N 180°E (Plates 5a, 5b), both model and TAO observations are fairly coherent with depth, indicative of a low vertical mode dominance in the temperature record. In fact the T/P assimilation is fairly successful in improving model temperature variations, where the assimilation resolves events more accurately in magnitude and timing, especially around days 700 and 1000.

At 0°N 95°W (Plates 5c, 5d), although TAO measurements display vertical coherence, the model does not, and in fact the assimilation results in a degradation of the estimate near the surface. This apparently is due to errors in the model's mean vertical stratification in the region. Figure 6 compares mean temperature profiles of the TAO data and model estimates. The thermocline is close to the surface towards the eastern

end of the Equatorial Pacific, and as a result stratification is fairly strong at the surface at 0°N 95°W. In comparison, due to its coarse resolution, the model thermocline is deeper and near surface stratification is weak. As a result, the model's temperature at the surface is dominated by changes associated with seasonal variations in vertical upwelling rather than intraseasonal vertical movement of the isotherms, resulting in the model's degradation.

At 2°S 165°E (Plates 5e, 5f), there is little improvement in temperature simulation both at the surface and depth even though mean vertical temperature stratification of model and data are comparable (Figure 6). However, the dominant signal in the in situ measurements are qualitatively lacking in the model estimates, indicative of model representation error. In fact, the in situ signal is incoherent over 375m depth suggesting the data being dominated by shorter vertical scales than what the model can resolve.

The spatial dependence of the assimilation's skill in resolving temperature changes is best analyzed using XBT data that provides a larger areal coverage. W.White has gridded monthly average near surface temperatures from historical XBT data (1955 to 1996), and its global extent is particularly convenient for comparison with present results. The gridded data set nominally covers the globe from 40°S to 60°N at 5° zonal and 2° meridional resolution with eleven depths between the surface and 400 m (Table 3). Comparisons are made during the modeling period by interpolating monthly averaged model fields onto the data grid.

The T/P assimilation is found to improve the model temperature simulation at most depths, but there is a tendency for the assimilation to degrade estimates at deeper levels of the XBT data. The model itself (simulation) has better skill in explaining observed temperature variability at shallower depths than at deeper levels, but this is primarily due to the dominance of seasonal heating and cooling and largely reflects the accuracy of COADS heat flux estimates (i.e., external forcing) rather than model dynamics per se. Plate 6 shows the spatial dependence of the assimilation's skill at four depths representative of the model resolution (Table 1). The largest degradation is found at 300m depth in the Equatorial Pacific, which dominates the overall statistics.

The degradation along the Equator at depth is apparently due to inaccuracies in the assimilation itself rather than due to model representation errors. Plates 5g and 5h compare temperature results at 0°N 140°W between 140m and 300m depths. Unlike other examples in Plate 5 that resulted in a degradation, the model simulation

is coherent with dominant variations measured by the mooring at both depths. Yet the assimilation degrades the estimate at 300m; in particular the largest degradation occurs between days 1100 and 1200. Interestingly, the difference between simulation (red) and assimilation (blue) are of opposite sign between 140m and 300m depths during this period; the assimilation (blue) is warmer than simulation (red) at 140m but is colder than simulation (red) at 300m. Such opposite changes are in the null space of the approximate filter/smoother (section 3) and therefore indicate a process not accounted for in the approximation. The changes of opposite sign are due to meridional advection of background stratification, whose meridional gradient is of opposite sign near the equator between 175m and 300m (Figure 7). The reduced-state filter assumes a closed dynamic system within the reduced-state (Fukumori and Malanotte-Rizzoli, 1995). However, temperature changes near the Equator as shown above indicate otherwise, violating the assumption underlying the approximation and leading to degradation and inconsistency of the assimilation.

5.5 Bottom Pressure Gauges

The barotropic circulation is best examined by bottom pressure measurements. Figure 8 shows the distribution of bottom pressure gauges available during the investigation period. Tidal signal was first removed from the hourly (in some cases 15 minute interval) bottom pressure data by the same University of Texas model used in correcting T/P measurements. Residual tidal fluctuations were further corrected by a least-squares fitting procedure at each station in addition to removing a linear trend to account for possible instrument drift. The result was then averaged by a running mean over twenty-four hours into pressure measurements every twelve hours.

Figure 9 shows a typical comparison near Crozet Island. Bottom pressure in the Southern Ocean is dominated by high frequency variations with time-scales as fast as a few days due to wind-driven barotropic motion (Fukumori et al., 1998). Model results are remarkably coherent with in situ measurements, which is a testament to the wind analysis' accuracy. Unlike baroclinic responses that depend on model stratification (Section 5.4), wind-driven barotropic response is less dependent on oceanic state, and therefore more accurately simulated by the model. Nevertheless, model discrepancies are evident and T/P assimilation does improve model estimates as evidenced in Figure 9b, in particular the lower frequencies (periods longer than approximately 50-days).

However, the assimilation lacks the skill in correcting the ultra-high frequency variations (periods less than 10-days), despite the model's coherence with in situ measurements. The limitation at high frequencies is in part due to the sampling period of the altimeter being 10 days.

Improvements are evidenced at most bottom pressure measurement sites, except three among the fifteen. Comparisons at these three sites, Dumont (65.6°S, 139.9°E), CD (58.4°S, 56.4°W), and Capetown (34.6°S, 17.8°E), are shown in Figure 10. Model results are qualitatively lacking the dominant variabilities seen at CD and Capetown, suggestive of dominating model representation errors. CD is in the middle of Drake Passage, and the fluctuations appear to be related to changes in the Antarctic Circumpolar Current, which the present simulation lacks the grid spacings to resolve. Variations at Capetown may be related to the Agulhas Current. Model results are in close agreement with pressure gauge records at Dumont. In fact, percentage-wise the simulation explains the largest fraction (56% of the data variance) of observed pressure variability at Dumont among all bottom pressure gauges. Apparently, the coarse state approximation of the region is not good enough to improve the model results any further; i.e., errors in the approximate filter/smoother outweigh improvements gained by the information extracted from altimetry.

6. Summary and Discussion

One of the primary virtues of data assimilation is its ability to estimate properties not directly measured. Such estimates could be of the same variable as assimilated but at a time and/or location where observations are not available, or of entirely different quantities. The accuracy of such estimates critically depends on the assumptions underlying the assimilation. If the assumptions are valid, an assimilation necessarily leads to a more accurate description of the ocean than without assimilation in every aspect of the solution. Two properties characterize the accuracy of the estimates; reliability and completeness.

Reliability concerns how meaningful estimates are and is closely related to the consistency of assumptions. Nothing new is learned if an assimilation is less accurate than without assimilation, and error estimates are not meaningful if they do not adequately measure the uncertainties of actual results. Completeness pertains to what the

estimates actually resolve and is related to the issue of model representation error. Assimilation provides estimates consistent with observations and models. However, model physics are incomplete due to truncation by the models' finite dimensions and/or approximations in the physics, thereby leaving processes that are real but are inconsistent with models and hence cannot be improved by assimilation.

The accuracy of an assimilation was examined in the context of analyzing satellite altimetric observations. Three-years of TOPEX/POSEIDON altimeter data from January 1993 to December 1995 were assimilated into a global, three-dimensional, non-linear primitive equation model. A time-asymptotic, reduced-state Kalman filter and smoother were employed. The filter and smoother's state reduction was achieved by including only the barotropic and first baroclinic modes in the estimate defined on a coarser horizontal grid than the forward model.

The reliability of the present estimates was demonstrated by statistical consistency checks as well as by improvements over corresponding simulated solutions against independent in situ observations, including sea level from tide gauges, current velocities from moorings, subsurface temperatures from XBTs and moorings, and pressures from bottom mounted pressure gauges. The magnitudes of the improvements were shown to be largely comparable with formal uncertainty estimates.

In some regions, however, inaccuracies in the estimate were identified, pointing to the violations of some of the assumptions. For instance, degradation in subsurface temperatures along the Equator was found to be due to inaccuracies in the reduced-state approximation. Namely, the dynamics of the chosen reduced state (barotropic plus first baroclinic modes) cannot be approximated as being a closed system near the Equator, thereby violating the validity of the reduced-state approximation. Nonlinear advection causes coupling of the reduced state space with shorter vertical scales that cannot be ignored. These inaccuracies accumulate over time, and in fact much of the degradation were found to occur towards the end of the 3-year analysis period.

Some of the increase in model-data differences after the assimilation were attributed to the dominating model representation errors. Over the short duration of the experiment, a large part of the model representation errors is correlated with the range space of the model, and therefore differences in model-data misfit is no longer necessarily an adequate measure of accuracy.

As evident from Eq (6), model representation error depends on the definition of model state. There are two categories in representation error; those intrinsic to the model itself and those due to the limitations associated with the specific reduced-state approximation. For the present study, the latter includes temperature errors associated with inaccuracies in the mean temperature profile (Plate 5c). Such errors can be reduced by including in the estimated state, diabatic processes controlling the model's mean hydrographic state, thereby changing the definition for the reduced-state.

It should be noted that as far as analyzing altimetric anomalies are concerned, the present adiabatic reduced state approximation is entirely consistent with the data used, and that the estimate's incomplete nature in hydrographic structure only becomes evident when compared with in situ measurements. Nonlinearities are not strong enough to adequately constrain the mean state of the ocean for the present model from altimetric anomalies alone.

7. Concluding Remarks

Proper prescription of model and data uncertainties are essential for data assimilation, as they define the estimation problem and thereby the quality of the solution. In particular identification of model representation error is important in understanding what exactly data assimilation resolves and hence is able to improve upon the results. An interesting question is to ascertain whether the missing physics included in representation errors are important at all in controlling the general circulation of the ocean. For instance, recent parameterization of eddy transports in terms of the large-scale property gradient appear to be sufficient in accounting for effects of eddy transport on the large-scale structure of the thermocline (e.g., Danabasoglu et al., 1994).

A consistent global assimilation of altimetric data is now feasible, but the accuracies of practical estimates are limited due to the insensitivities of the assimilation to some of the uncertainties of the model circulation. Other observations, in particular, in situ data are essential in further constraining the model. Synthesis of various observations using models will likely be an iterative process of trial and error. While withholding observations as was performed in this study, as opposed to assimilating all data at once, is not fundamental for checking consistencies, testing the validity of fewer assumptions (in particular data error) at a time by withholding subsets of data

may more readily identify the source of inconsistencies. Every aspect of a model estimate is improved by assimilation only if all assumptions are valid. The challenge lies in identifying the exact nature and property of model uncertainties that are central to leading assumptions of data assimilation.

Acknowledgment

References

Anderson, D. L. T., J. Sheinbaum, and K. Haines, 1996. Data assimilation in ocean models, *Reports on Progress in Physics*, **59**, 1209–1266.

Bennett, A. F., 1992. "Inverse methods in physical oceanography", Cambridge University Press, Cambridge, U.K., 346pp.

Bretherton, F. P., R. E. Davis, and C. B. Fandry, 1976. A technique for objective analysis and design of oceanographic experiments applied to MODE–73, *Deep-Sea Research*, **23**, 559–582.

Cane, M. A., A. Kaplan, R. N. Miller, B. Tang, E. C. Hackert, and A. J. Busalacchi, 1996. Mapping tropical Pacific sea level: Data assimilation via a reduced state space Kalman filter, *Journal of Geophysical Research*, **101**, 22,599–22,617.

Chao, Y., and L.-L. Fu, 1995. A comparison between the TOPEX/POSEIDON data and a global ocean general circulation model during 1992–1993, *Journal of Geophysical Research*, **100**, 24,965–24,976.

Danabasoglu, G., J. C. McWilliams, and P. R. Gent, 1994. The role of mesoscale tracer transports in the global ocean circulation, *Science*, **264**, 1123–1126.

da Silva, A. M., C. C. Young, and S. Levitus, 1994. Atlas of Surface Marine Data 1994, Volume 3: Anomalies of Heat and Momentum Fluxes, NOAA Atlas NESDIS 8. U.S. Dept. Commerce, NOAA, NESDIS.

Eanes, R., and S. Bettadpur, The CSR3.0 global ocean tide model: Diurnal and semi-diurnal ocean tides from TOPEX/POSEIDON altimetry, *CSR-TM-96-05*, Univ. Of Tex. Cent. for Space Res., Austin, Texas.

Evensen, G., 1994. Sequential data assimilation with a nonlinear quasi-geostrophic model using Monte Carlo methods to forecast error statistics, *Journal of Geophysical Research*, **99**, 10143–10162.

Ezer, T., and G. L. Mellor, 1994. Continuous assimilation of Geosat altimeter data into a three-dimensional primitive equation Gulf Stream model, *Journal of Physical Oceanography*, **24**, 832–847.

Fu, L.-L., I. Fukumori and R. N. Miller, 1993. Fitting dynamic models to the Geosat sea level observations in the Tropical Pacific Ocean. Part II: A linear, wind-driven model, *Journal of Physical Oceanography*, **23**, 2162–2181.

Fukumori, I., J. Benveniste, C. Wunsch and D. B. Haidvogel, 1993. Assimilation of sea surface topography into an ocean circulation model using a steady-state smoother, *Journal of Physical Oceanography*, **23**, 1831–1855.

Fukumori, I., and P. Malanotte-Rizzoli, 1995. An approximate Kalman filter for ocean data assimilation; An example with an idealized Gulf Stream model, *Journal of Geophysical Research*, **100**, 6777–6793.

Fukumori, I., 1995. Assimilation of TOPEX sea level measurements with a reduced-gravity shallow water model of the tropical Pacific Ocean, *Journal of Geophysical Research*, **100**, 25027–25039.

Fukumori, I., R. Raghunath, and L. Fu, 1998. The nature of global large-scale sea level variability in relation to atmospheric forcing: A modeling study, *Journal of Geophysical Research*, **103**, 5493–5512.

Gelb, A., 1974. "Applied Optimal Estimation", M.I.T. Press, Cambridge, MA 374 pp.

Ghil, M., and P. Malanotte-Rizzoli, 1991. Data assimilation in meteorology and oceanography, *Advances in Geophysics*, **33**, 141–266.

23

Giering, R., and T. Kaminsky, 1998. Recipes for adjoint code construction, *ACM Transactions on Mathematical Software*, (in press).

Gill, A. E., 1982. "Atmosphere–Ocean Dynamics", Academic Press, San Diego, CA, 662pp.

Gill, A. E., and P. P. Niiler, 1973. The theory of the seasonal variability in the ocean, *Deep–Sea Research*, **20**, 141–177.

Haines, K., 1991. A direct method for assimilating sea surface height data into ocean models with adjustments to the deep circulation, *Journal of Physical Oceanography*, **21**, 843–868.

Halpern, D., R. A. Knox, and D. S. Luther, 1988. Observations of 20-day period meridional current oscillations in the upper ocean along the Pacific Equator, *Journal of Physical Oceanography*, **18**, 1514–1534.

Hellerman, S., and M. Rosenstein, 1983. Normal monthly wind stress over the world ocean with error estimates, *Journal of Physical Oceanography*, **13**, 1093–1104.

Levitus, S., 1982. Climatological Atlas of the World Ocean, Professional Papers, vol. 13, National Oceanic and Atmospheric Administration, Rockville, MD.

Menemenlis, D., and M. Chechelnitsky, 1998. Error estimates for an ocean general circulation model from altimeter and acoustic tomography data, (unpublished manuscript).

Miller, R. N., and M. A. Cane, 1989. A Kalman filter analysis of sea level height in the tropical Pacific, *Journal of Physical Oceanography*, **19**, 773–790.

Mitchum, G. T., 1994. Comparison of TOPEX sea surface heights and tide gauge sea levels, *Journal of Geophysical Research*, **99**, 24,541–24,553.

Pacanowski, R., and S. G. H. Philander, 1981. Parameterization of vertical mixing in numerical models of tropical oceans, *Journal of Physical Oceanography*, **11**, 1443–1451.

Pacanowski, R., K. Dixon, and A. Rosati, 1991. Modular Ocean Model Users' Guide, Ocean Group Tech. Rep. 2, Geophys. Fluid Dyn. Lab., Princeton, N.J..

Pinardi, N., A. Rosati, and R. C. Pacanowski, 1995. The sea surface pressure formulation of rigid lid models. Implications for altimetric data assimilation studies, *Journal of Marine Systems*, **6**, 109–119.

Ponte, R. M., 1993. Variability in a homogeneous global ocean forced by barometric pressure, *Dynamics of Atmospheres and Oceans*, **18**, 209–234.

Sasaki, Y., 1970. Some basic formalisms in numerical variational analysis, *Monthly Weather Review*, **98**, 875–883.

Slutz, R. J., S. J. Lubker, J. D. Hiscox, S. D. Woodruff, R. L. Jenne, D. H. Joseph, P. M. Steurer and J. D. Elms, 1985. COADS, Comprehensive Ocean-Atmosphere Data Set, Release 1. Climate Research Program, Environmental Research Laboratory, Boulder, CO, 262pp.

Stammer, D., C. Wunsch, R. Giering, Q. Zhang, J. Marotzke, J. Marshall, and C. Hill, 1997. The global ocean circulation estimated from TOPEX/POSEIDON altimetry and the MIT general circulation model, Report No. 49, Center for Global Change Science, Massachusetts Institute of Technology, Cambridge, MA, 40pp.

Stengel, R. F., 1986. "Stochastic Optimal Control", A Wiley-Interscience publication, New York, NY, 638pp.

Woodruff, S. D., R. J. Slutz, R. L. Jenne, and P. M. Steurer, 1987. A comprehensive ocean-atmosphere data set, *Bulletin of the American Meteorological Society*, **68**, 1239–1250.

Wu, J., 1982. Wind stress coefficients over sea surface from breeze to hurricane, *Journal of Geophysical Research*, **87**, 9704–9706.

Wunsch, C., 1996. "The Ocean Circulation Inverse Problem", Cambridge Univ. Press, New York, NY, 442pp.

Table Legends

Table 1: Depth of levels (z) and layer thicknesses (Δz) used in the model. Units are in meters.

Table 2: Comparison of daily velocity anomalies measured by TOGA TAO moorings and model estimates interpolated to corresponding current meter locations. Correlations and residual variances (cm^2/s^2) with respect to current meter measurements (TAO) are given for model simulation (sim) and T/P assimilation (assim). Also listed are the respective velocity variances. The two numbers under each heading correspond to zonal and meridional components of velocity, respectively. Numbers in parenthesis for the simulation denote estimates that have statistically insignificant correlations (at 95% confidence) with current meter measurements or residual variances larger than measurement variances indicating lack of skill. Numbers in parenthesis for the assimilation denote estimates that have less skill than the simulation.

Table 3: A summary of comparing global monthly gridded temperature observations and model estimates. Values shown are global averages. Numbers in parentheses for the simulation indicate estimates with larger residual differences than the data variance themselves. Numbers in parenthesis for the assimilation denote estimates that have less skill than the simulation.

Figure Legends

Figure 1: Model coastline (thick) and bottom topography (thin). Contour interval for topography is 1000 m.

Figure 2: Structures of sea level resolution. Contours describe particular columns of the sea level resolution matrix based on the dominant 300 EOFs. The resolutions correspond to sea level at the large center asterisk in respective figures; (a) 172°W 35°N, (b) 152°W 0°N. Contour intervals are 4.4×10^{-3} (A) and 1.7×10^{-3} (B), respectively in arbitrary units (the sum of squared values over the globe is by definition one.). The coarse grid defining the approximate filter is denoted by the smaller asterisks.

Figure 3: Coarse representation of model sea level anomaly. The model sea level (a) is transformed to the coarse grid (b) by the horizontal mapping operator discussed in Secion 2. Sea level is that of March 16, 1995 (1992 day 1170). Contour interval is 5 cm. Solid (dashed) curves denote positive (negative) values.

Figure 4: Examples of Kalman gain's horizontal structure corresponding to a 1 cm sea level difference between data and model at the asterisk. Contours are barotropic mass transport stream function (a, b), and temperature (c, d at 1700 m and 175 m depth, respectively). Contour intervals are 2×10^{-10} cm^3/s for (a) and (b), and 4×10^{-6} and 4×10^{-4} °C for (c) and (d), respectively. Positive numbers are shown in solid contours with the first positive contour equaling half the contour interval in magnitude. Arrows in each figure are barotropic (a, b) and baroclinic (c, d) velocities, respectively, with reference vectors shown separately for each panel. To reduce clutter, only a subset of vectors are shown where values are relatively large. The assumed data locations are (a) 60S 170W, (b) 20N 60W, (c) 60S 170W, and (d) 0N 170W. Corresponding effects on sea level at the data points are 0.02, 0.02, 0.002, and 0.03 cm for (a), (b), (c), and (d), respectively.

Figure 5: Locations of tide gauge stations used in validating model estimates (a). Open circles denote gauges which agree better with T/P assimilated estimate than simulation without assimilation as measured by residual magnitudes. Also shown in (b) by open (closed) circles are stations with significant (insignificant) correlation with T/P data used in this study at the 95% confidence.

Figure 6: Mean vertical temperature profile at 0°N 95°W (a) and 2°S 165°E (b). Circles (thick line) and asterisks (thin line) denote averages of TAO and smoothed estimates, respectively.

Figure 7: Mean meridional model temperature profile along 140°W.

Figure 8: Location of bottom pressure gauges used in model-data comparison. The circles (asterisks) denote gauges with smaller (larger) model-data difference after T/P assimilation.

Figure 9: Bottom pressure near Crozet Island 46°S 52°E. Days 475 to 550 is expanded in (b) to show details. Different curves are in situ measurement (black), simulation (gray dashed), and T/P assimilation (gray solid). The upper plot does not show the simulation to reduce clutter. The model-data residuals for the simulation and assimilation are 11.0 and 8.5 mbar^2, respectively.

Figure 10: Bottom pressure at 58.4°S 56.4°W (a), Capetown 34.6°S 17.8°W (b), and Dumont 65.6°S 139.9°E. The model-data residuals (mbar^2) (simulation, assimilation) are (a) (22.9, 23.1), (b) (3.8, 4.1), (c) (5.2, 6.1), respectively.

Plate Legends

Plate 1: Error Calibration; (a) estimate of effective data error of the reduced-state filter (Eq 19), (b) model simulation error estimate (sea level) (Eq 18), (c) calibrated (zonal) wind stress error, (d) model simulation error (sea level) based on (c). See text for details.

Plate 2: Sea level anomaly (cm) associated with Kalman filter changes in model state corresponding to an instantaneous 1 cm model-data difference; (a) baroclinic displacement, (b) barotropic circulation. The estimates are strictly local reflecting sea level difference at each separate grid point.

Plate 3: Differences of model-data residuals; (a) simulation minus forecast, (b) expected value of (a), (c) forecast minus analysis, (d) expected valued of (c). Values are root-mean-square differences of model-data residual variances. The sign is as indicated above; e.g., positive values in (a) indicates larger simulation residual than forecast residual. Units in cm.

Plate 4: Comparison of velocity anomalies (cm/s) at select TAO current meters. The figures compare zonal velocities at 45m 140°W (a), 45m 110°W (b), and 120m 110°W (c), and meridional velocity at 25m 140°W (d). The different curves are TAO measurements (black), model simulation (red), and T/P assimilation (blue). Anomalies are relative to the respective temporal means. The red and blue bars denote simulated and smoothed model state error estimates, respectively, computed as part of the Kalman filter.

Plate 5: Comparison of temperature anomalies (°C) at select TAO measurements; (a) 200m 8°N 180°E, (b) 500m 8°N 180°E, (c) 20m 0°N 95°W, (d) 300m 0°N 95°W, (e) 125m 2°S 165°E, (f) 500m 2°S 165°E, (g) 140m 0°N 140°W, (h) 300m 0°N 140°W. Different curves are TAO measurements (black), model simulation (red), and T/P assimilation (blue). Anomalies are relative to respective temporal means. The red and blue bars denote simulated and smoothed model state error estimates, respectively, computed as part of the Kalman filter. The model-data residual variances (simulation, smoothed) (°C^2) are (a) (0.23, 0.10), (b) (0.027, 0.021), (c) (3.0, 3.3), (d) (0.28, 0.24), (e) (1.8, 2.0), (f) (0.25, 0.30), (g) (1.9, 1.7), (h) (0.30, 0.61).

Plate 6: Differences of simulation minus assimilation residual variances with respect to gridded XBT data at four representative depths; (a) 20m, (b) 80m, (c) 160m, (d) 300m. Units in °C^2. Negative values indicate that assimilation is further away from the measurements than simulation is.

	z(m)	Δz
1	25	50
2	75	50
3	175	150
4	325	150
5	550	300
6	850	300
7	1200	400
8	1700	600
9	2375	750
10	3250	1000
11	4250	1000
12	5250	1000

Table 1

Depth (m)	Variance			Correlation		Residual Variance	
	TAO	sim	T/P assim	sim	T/P assim	sim	T/P assim
165° E							
10	1030.1, 381.3	289.5, 84.1	291.5, 77.5	0.44, 0.23	0.57, (0.21)	835.6, (384.3)	701.8, (385.4)
50	733.2, 323.9	145.5, 40.7	158.6, 39.5	0.45, 0.29	0.61, 0.29	585.9, 299.0	473.1, 297.5
100	715.4, 433.2	67.9, 27.0	91.6, 26.8	(0.13), 0.24	0.39, 0.27	(725.4), 407.9	608.1, 402.7
150	288.0, 162.2	42.4, 19.1	77.0, 17.6	0.53, 0.24	0.76, 0.31	212.6, 154.4	138.0, 146.5
200	105.5, 134.9	66.6, 10.3	113.1, 10.6	0.59, 0.32	(0.53), (0.29)	72.8, 121.1	(102.3), (123.2)
250	128.1, 134.2	32.0, 9.9	53.8, 9.0	0.45, 0.30	(0.35), 0.33	101.9, 122.0	(124.2), 120.0
140° W							
10	1230.9, 884.5	555.0, 33.7	457.9, 43.8	0.40, (0.09)	0.50, (0.03)	1120.1, (885.5)	944.3, (916.9)
25	1073.9, 781.5	590.0, 32.8	512.4, 43.3	0.43, (0.04)	0.55, (0.01)	975.4, (800.0)	772.1, (821.9)
45	1137.6, 665.1	351.0, 17.1	329.7, 26.2	0.38, (0.08)	0.60, (0.02)	1013.1, (665.5)	735.4, (686.6)
80	1396.2, 471.9	158.7, 16.6	162.5, 27.1	0.14, (0.10)	0.37, (0.01)	(1420.1), 470.6	1208.9, (497.1)
120	325.0, 197.7	95.0, 7.5	150.1, 11.3	0.45, 0.20	0.53, (0.16)	260.9, 189.8	240.7, (194.2)
200	179.4, 128.0	140.5, 9.0	139.1, 10.5	0.20, (0.04)	0.32, 0.13	(257.8), (134.3)	216.7, 129.0
110° W							
10	1635.8, 940.3	163.2, 32.5	229.7, 36.2	0.48, 0.20	(0.44), (0.19)	1300.9, 904.3	(1332.0), (905.9)
25	1839.5, 1008.3	153.3, 33.5	221.6, 39.7	0.50, 0.16	(0.33), 0.18	1464.2, 983.7	(1641.4), 977.9
45	2269.0, 615.4	106.1, 12.5	183.0, 18.6	0.47, 0.18	(0.23), 0.19	1914.8, 596.8	(2154.6), 593.2
80	660.0, 319.1	70.3, 17.7	187.5, 23.6	0.32, (0.09)	(0.30), 0.09	591.7, (323.4)	(638.4), (327.8)
120	393.7, 180.7	49.6, 8.3	145.8, 12.1	0.45, (0.06)	0.55, 0.08	316.9, (184.3)	274.8, (185.7)
200	311.0, 225.4	56.4, 4.4	117.3, 6.9	0.27, (0.02)	0.39, 0.06	294.8, (228.5)	280.0, 227.9

Table 2

Depth	Variance			Residual		Correlation	
(m)	XBT	sim	assim	sim	assim	sim	assim
0	3.12	1.13	1.04	1.88	1.82	0.59	0.60
20	2.77	1.13	1.04	1.62	1.55	0.61	0.62
40	1.71	1.09	1.01	1.06	0.98	0.61	0.63
60	1.08	1.06	0.97	1.00	0.89	0.55	0.58
80	0.87	0.97	0.88	(1.09)	0.97	0.42	0.45
120	0.63	0.44	0.39	(0.72)	0.66	0.23	0.26
160	0.39	0.24	0.23	(0.40)	0.37	0.28	0.31
200	0.22	0.20	0.20	(0.27)	0.26	0.29	0.30
240	0.14	0.14	0.14	(0.18)	0.18	0.28	0.29
300	0.10	0.11	0.12	(0.15)	(0.15)	0.27	0.27
400	0.08	0.06	0.07	(0.11)	(0.11)	0.24	(0.23)

Table 3

80N
40N
0
40S
80S
0   90E   180   90W   0

(a)

(b)

(A)

(B)

3

0.01 cm/s

(a)

0.01 cm/s

(b)

0.001 cm/s

(c)

0.05 cm/s

(d)

4
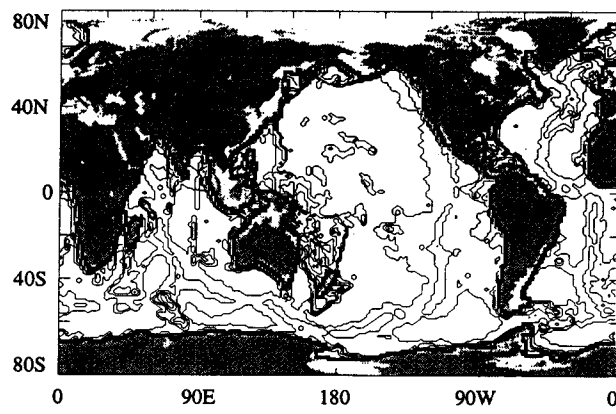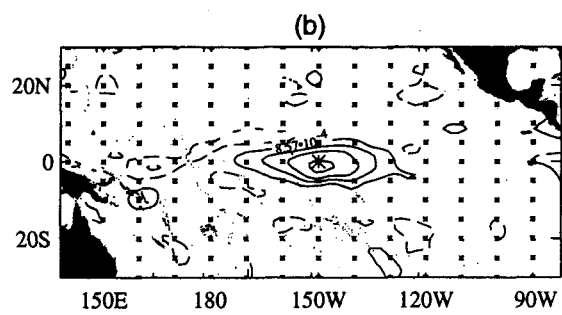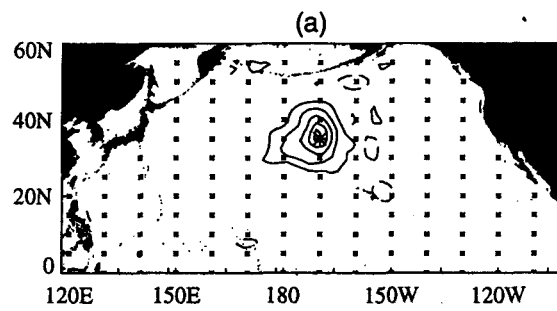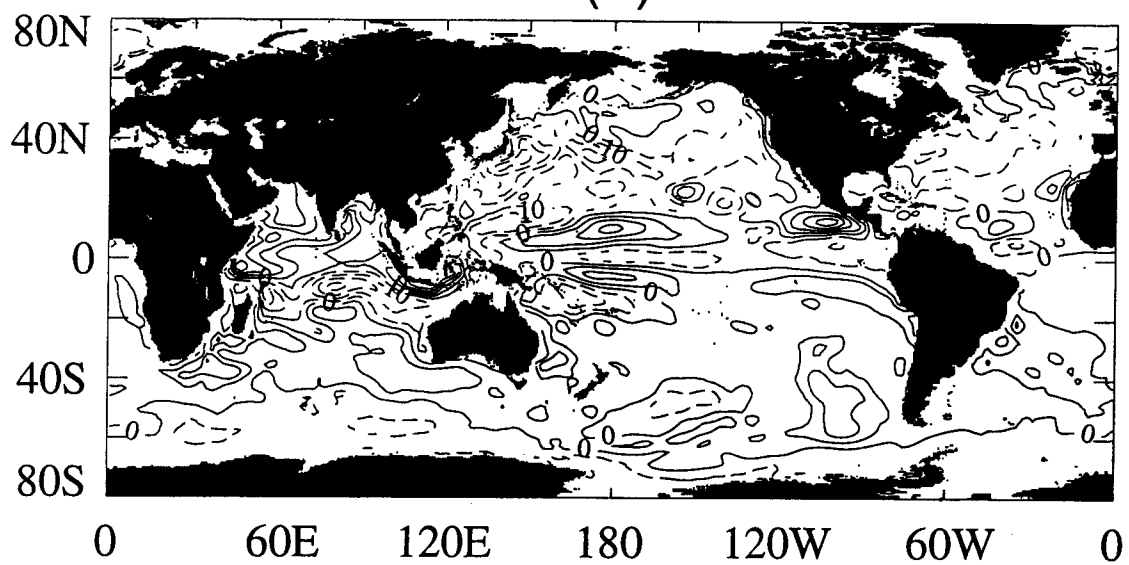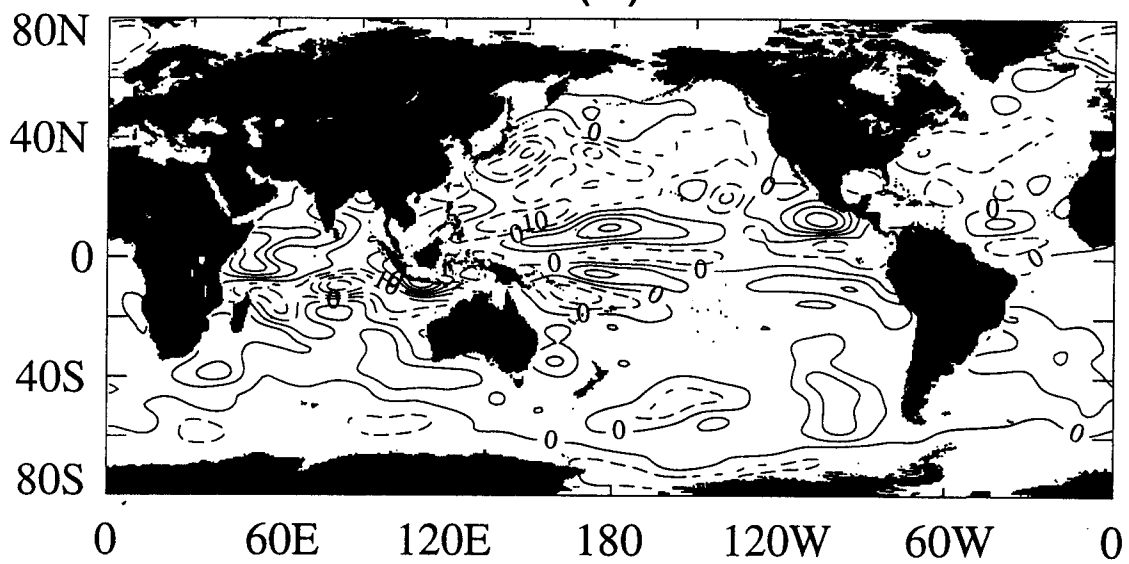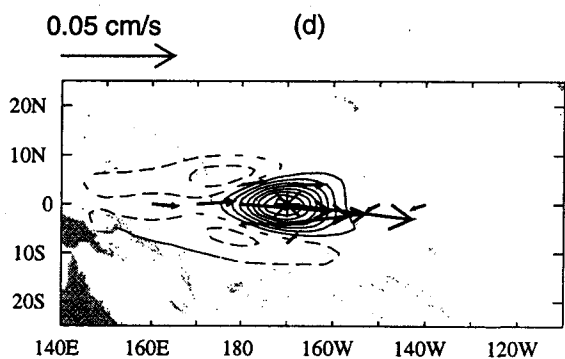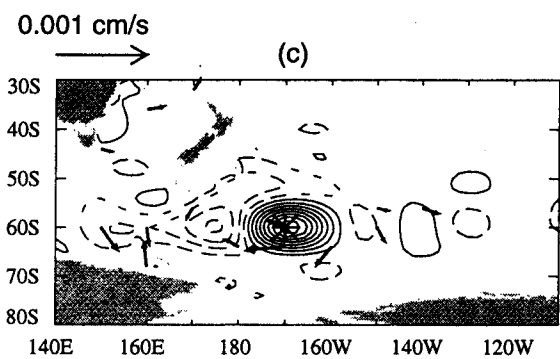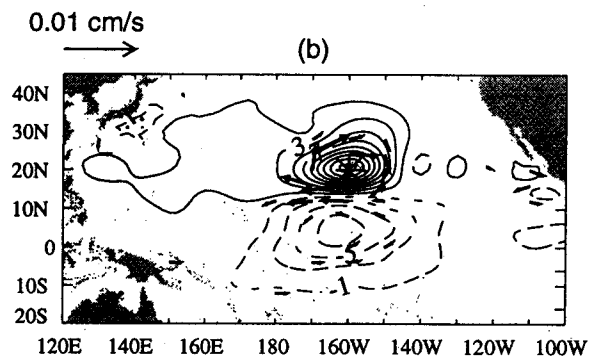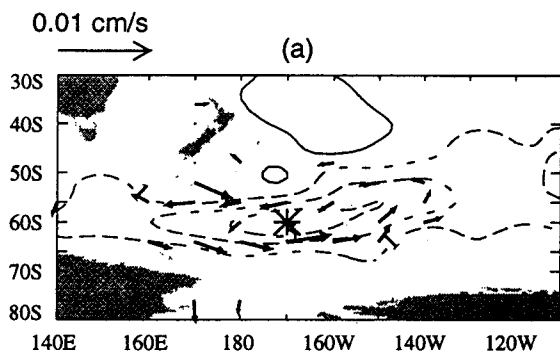
(a) Tide gauge vs T/P smoothed estimate
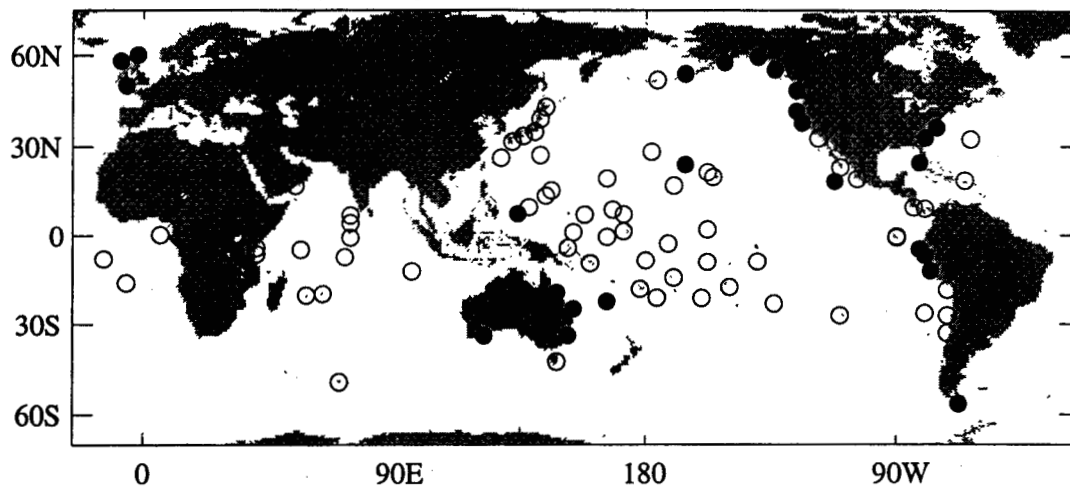
(b) Tide gauge vs T/P data
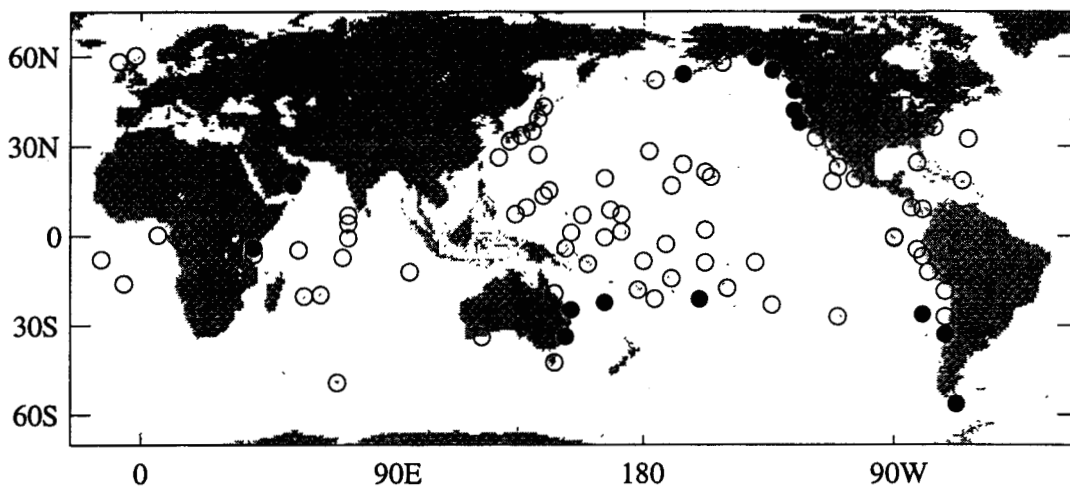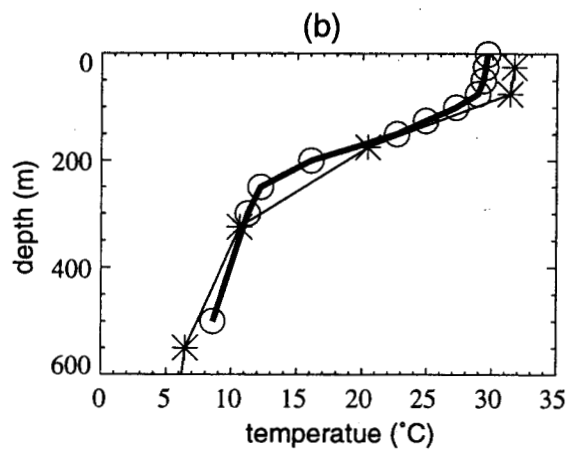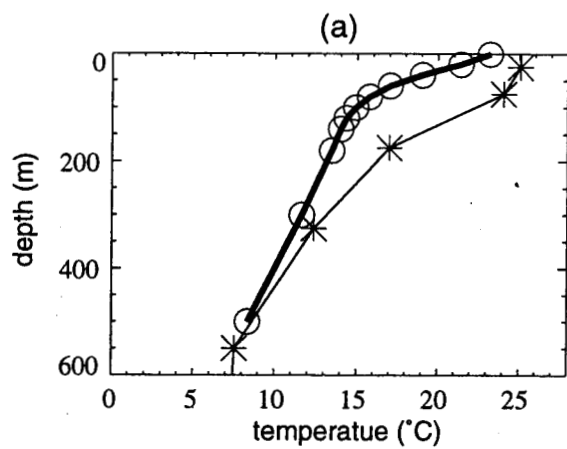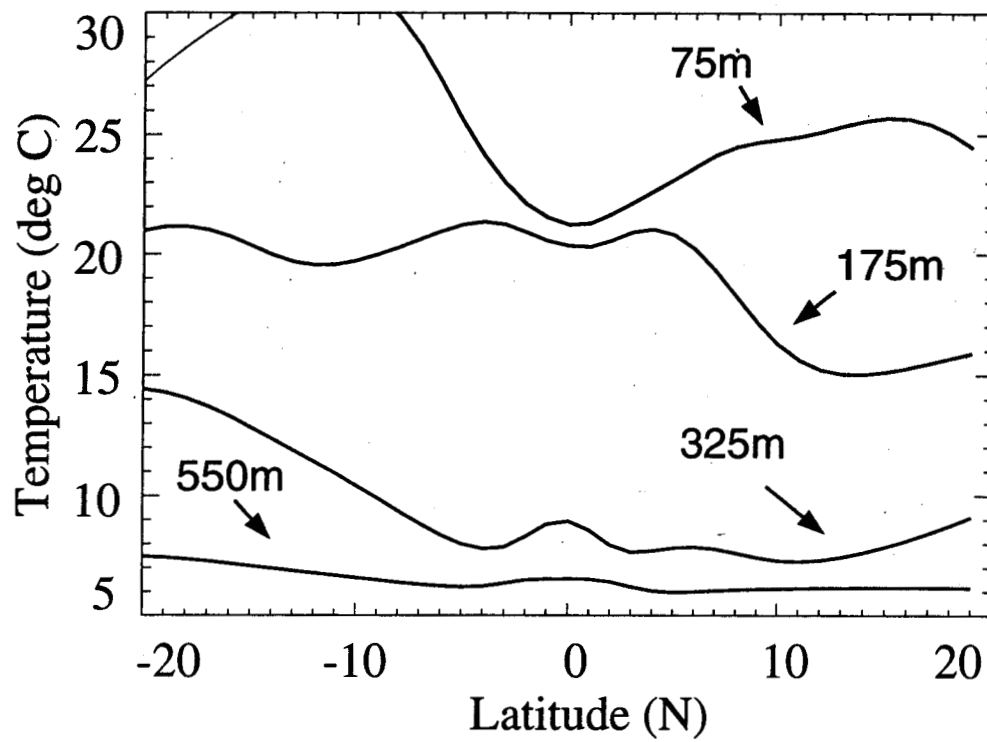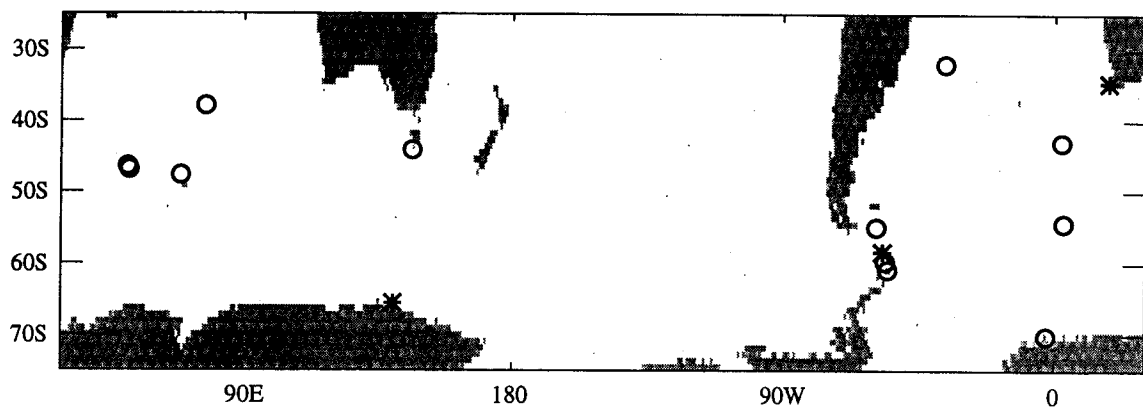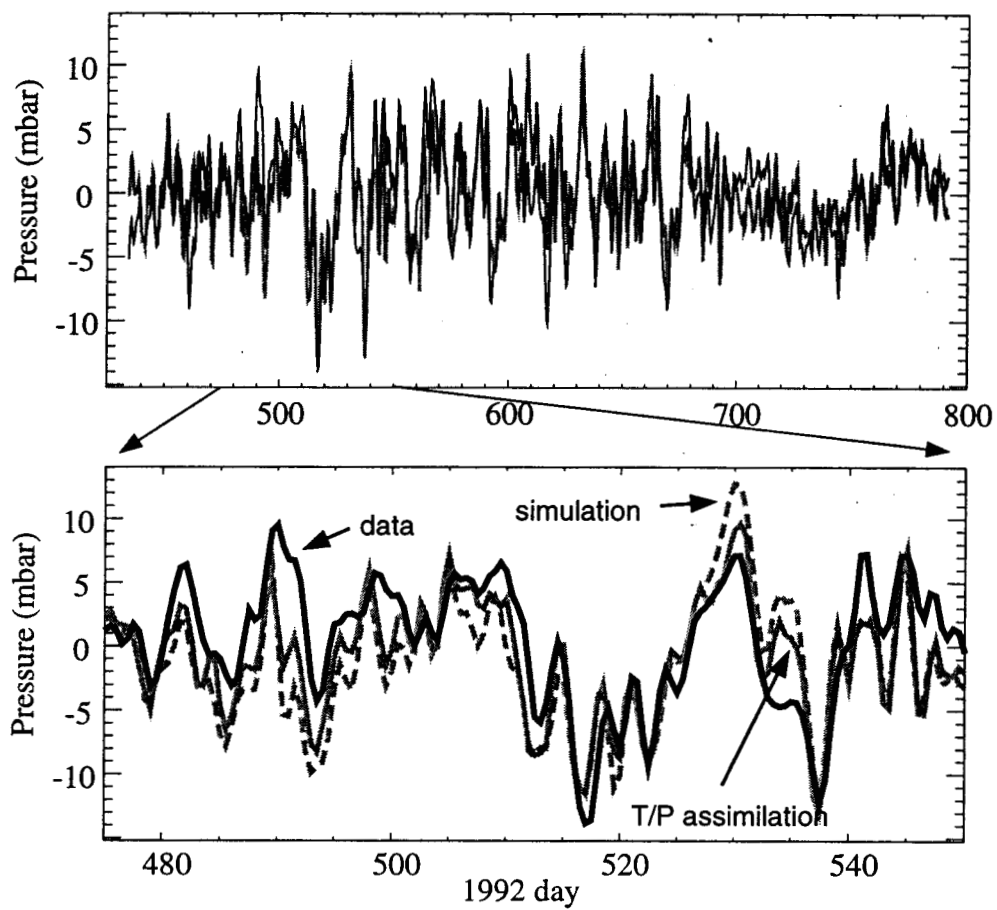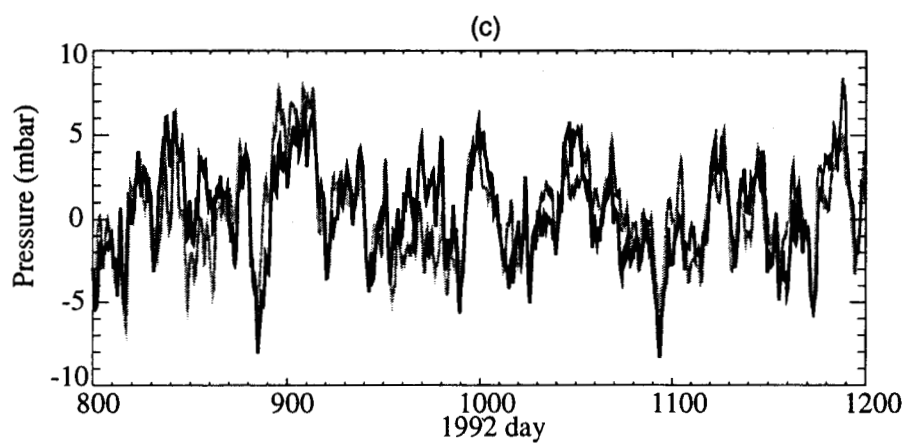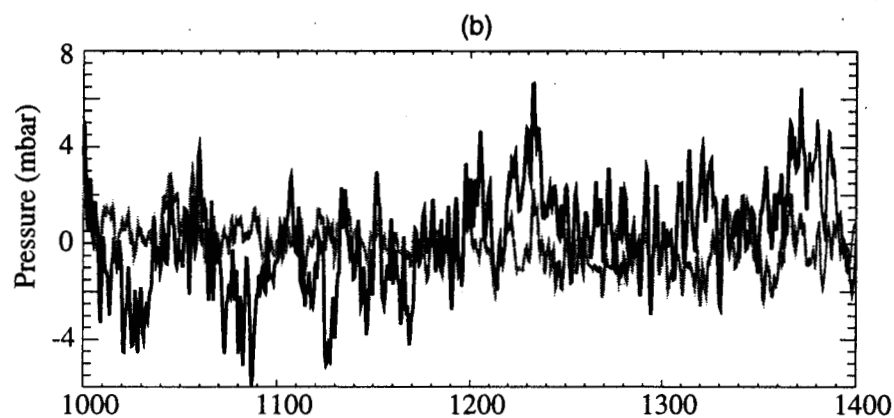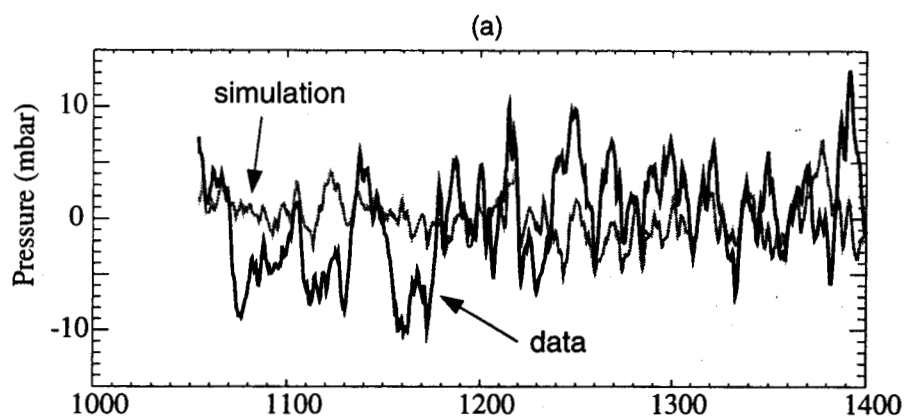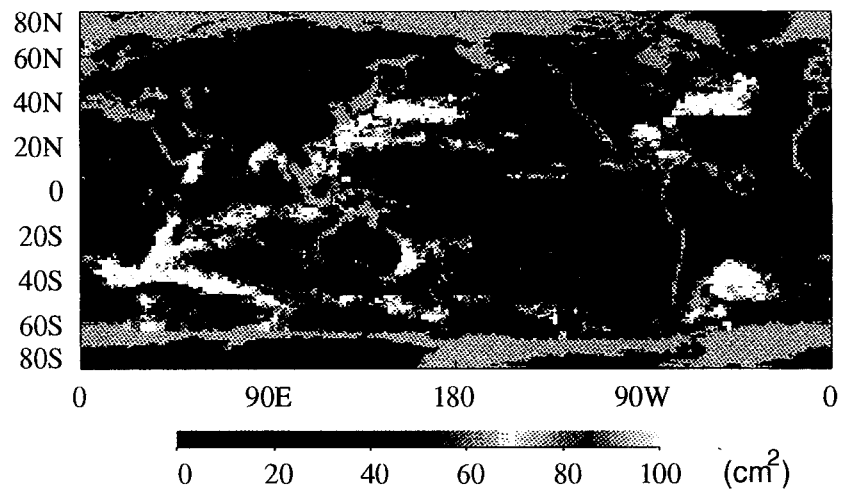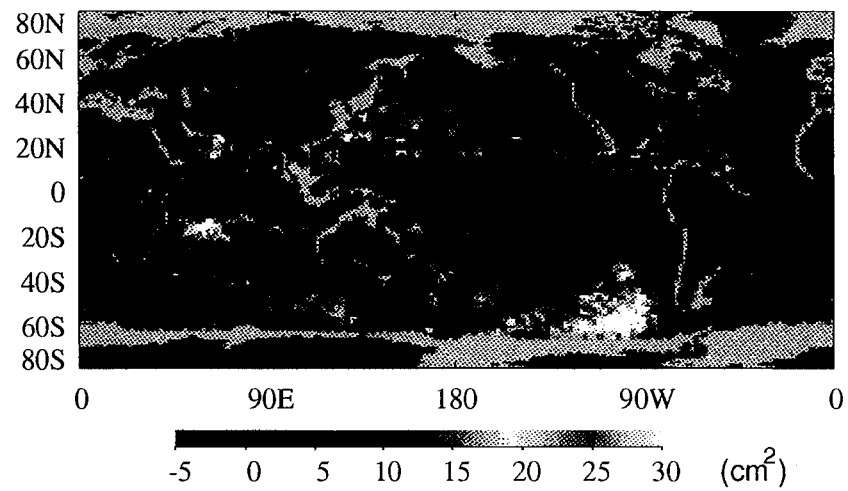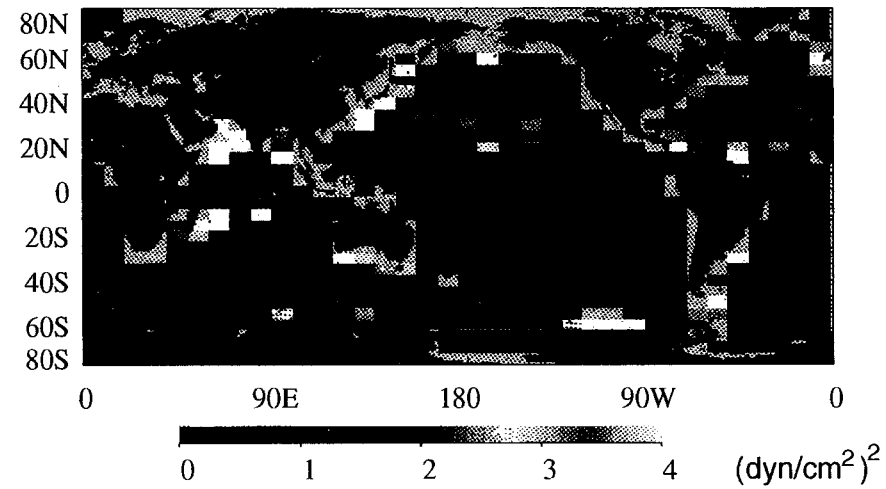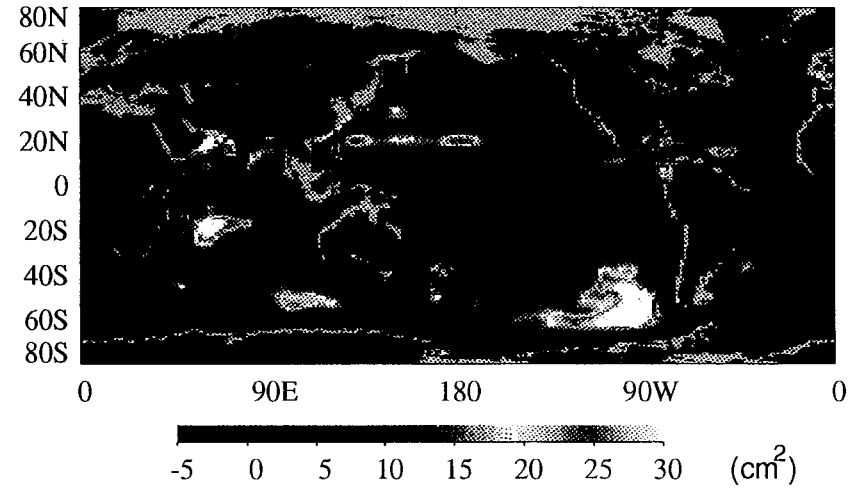
(a)

(b)

6

Mean Temperature profile along 140W

7

9

(a)

(b)

(c)

1992 day

(a)

(b)

(c)

(d)

Plate 1

(A) Baroclinic contribution

80N
60N
40N
20N
0
20S
40S
60S
80S

0   90E   180   90W   0

0.00   0.02   0.04   0.06   0.08   0.10
sea level (cm)

(A) Baroclinic contribution

80N
60N
40N
20N
0
20S
40S
60S
80S

0   90E   180   90W   0

0.00   0.02   0.04   0.06   0.08   0.10
sea level (cm)

Plate 2

Plate 3

(a)

(b)

(c)

(d)

1992 day

Plate 4

(a)

(b)

(c)

(d)

(e)

(f)

(g)

(h)
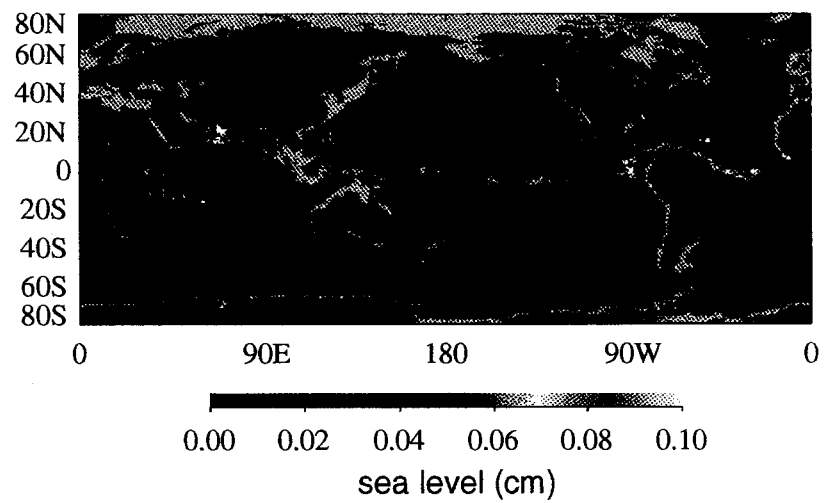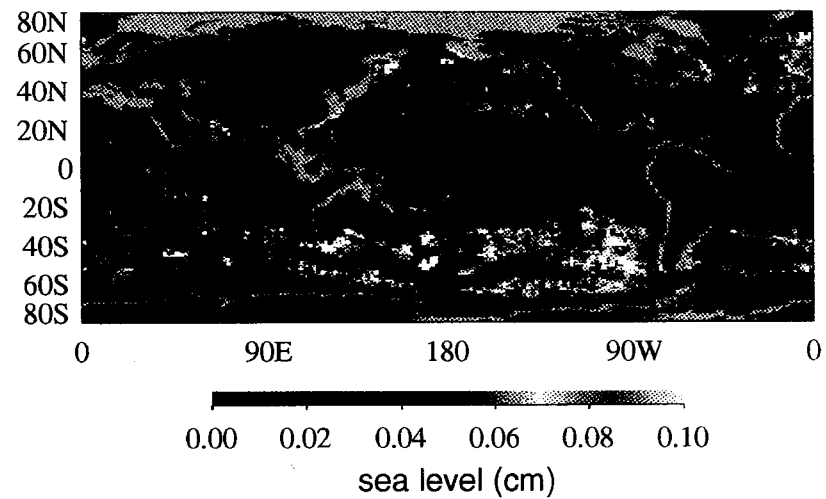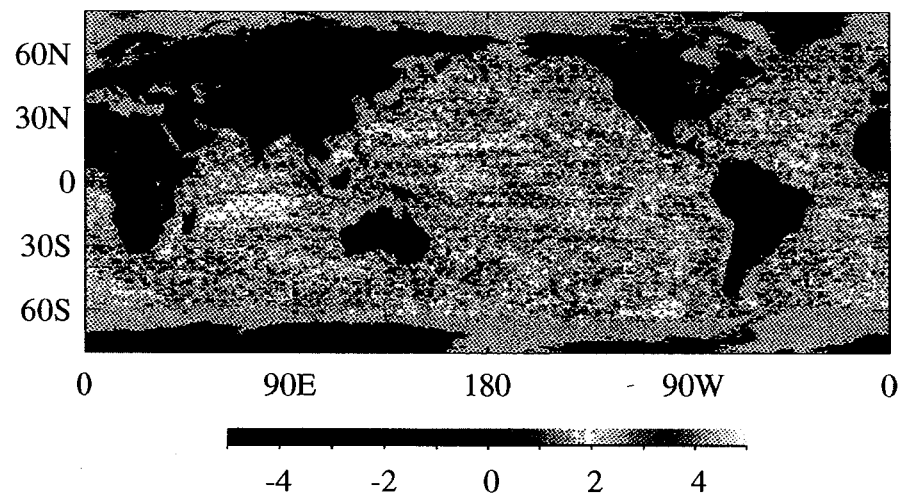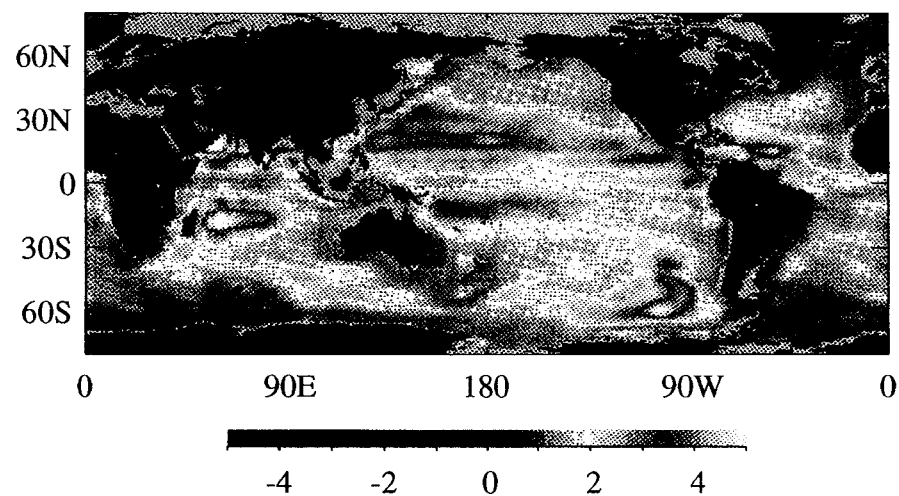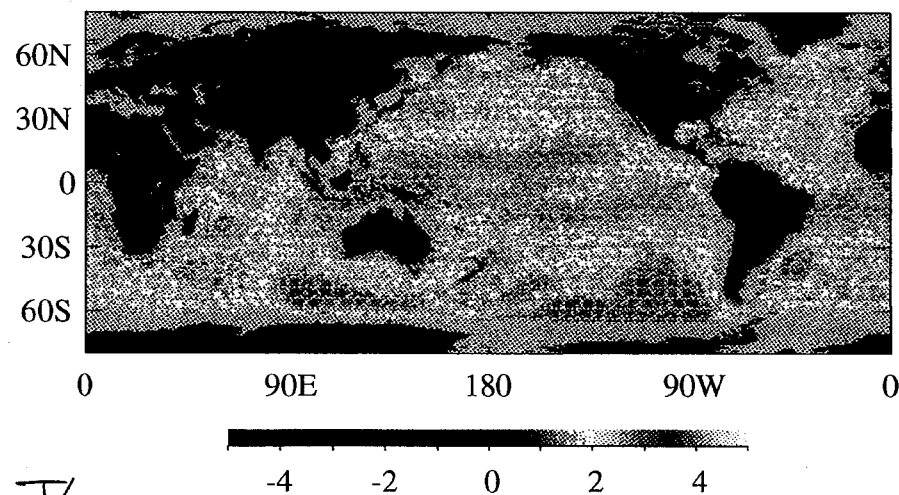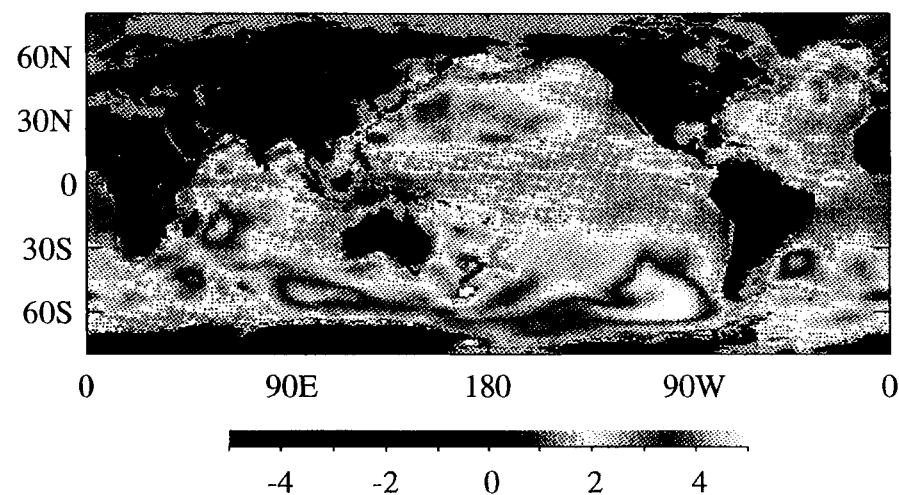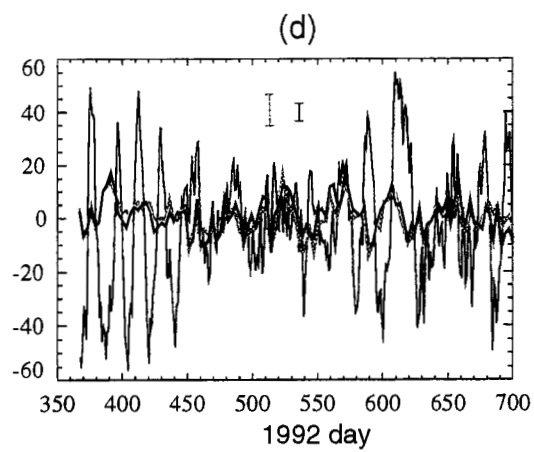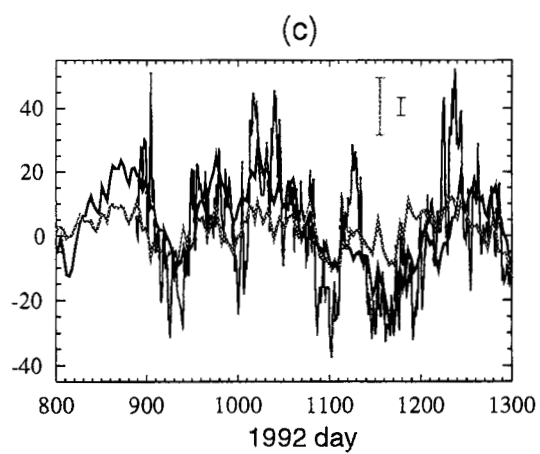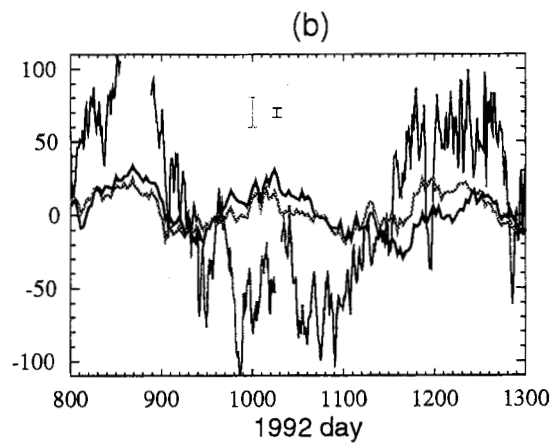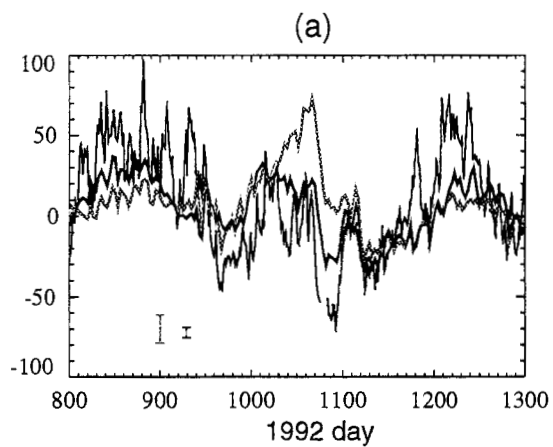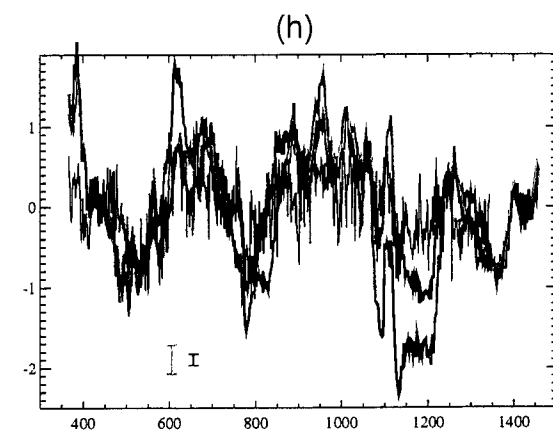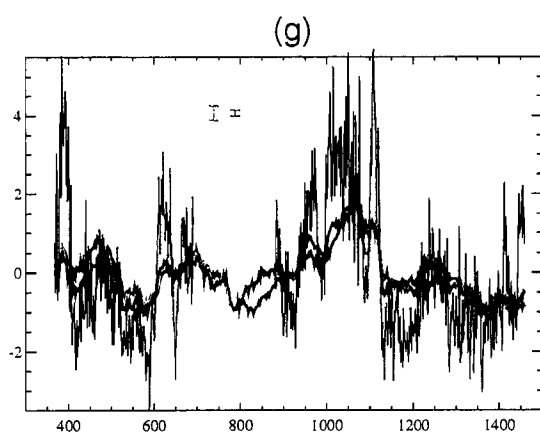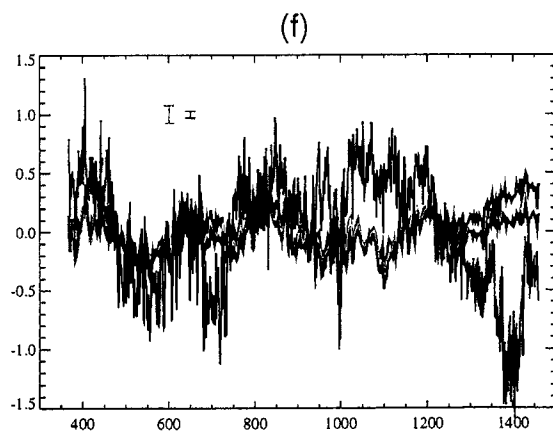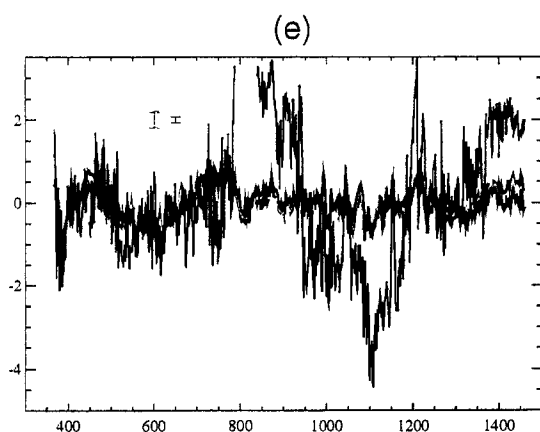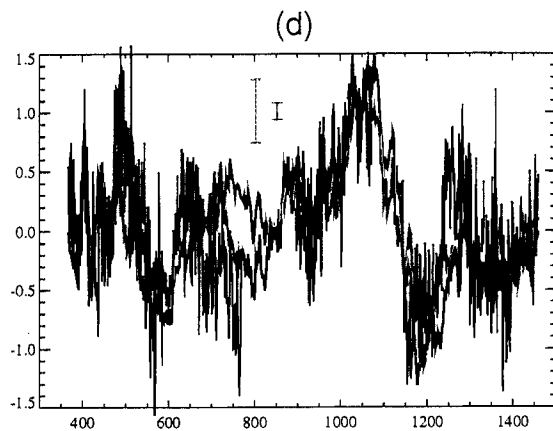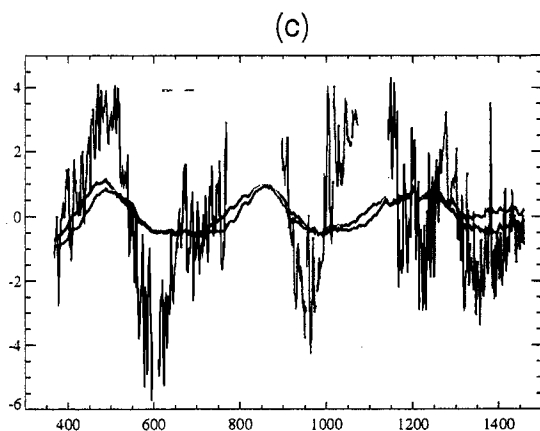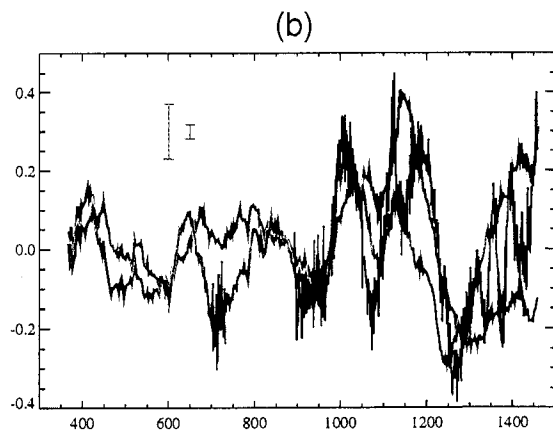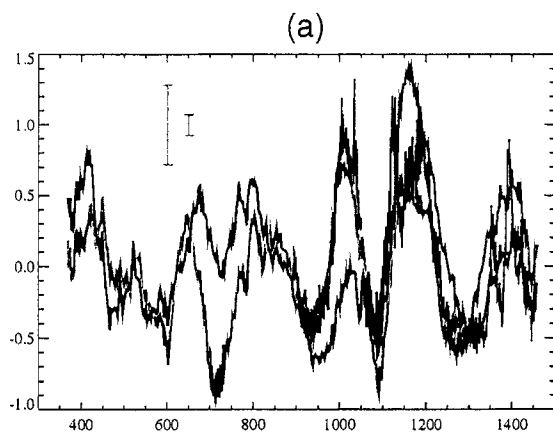
Plate 5

(A) 20 m

(B) 80 m

(C) 160 m

(D) 300 m

Plate 6